Chapter 2

"IN SITU" MEASUREMENT TECHNIQUES FOR IONOSPHERIC-THERMOSPHERIC INVESTIGATIONS

Edward P. Szuszczewicz
Laboratory for Atmospheric and Space Sciences
Science Applications International Corporation
McLean, Virginia 22102

Abstract

Advances in our understanding of coupled ionospheric and thermospheric responses to energetic inputs are currently limited by an inadequate database. Major problems include the complex interplay of thermospheric winds and electric fields in the Earth's electrodynamic circuit, the lack of routine access to detailed diagnostics of winds, electric fields, electron density distributions and ion composition in the lower ionosphere, and incomplete parameter coverage of cause-effect terms as a function of seasonal, diurnal, solar cycle and geomagnetic controls. "In situ" measurements can provide opportunities for a comprehensive database on the state and condition of the coupled system and the causal mechanisms. These measurements can diagnose the full spectrum of possibilities from the quiescent macroscale domain down to meter- scale irregularity structures known to populate the ionosphere in its most disturbed condition. Aspects of these micro- and macroscale features are reviewed with a perspective intended to develop an understanding of required "in situ" measurement capabilities; and a number of diagnostic techniques are described which form a baseline complement for a rocket or satellite payload. The discussion focuses on traditional techniques which have had broad applications and cover the spectrum of measurements from thermal plasma diagnostics to thermospheric winds and energetic particle spectrometry, with some discussion of limitations, future needs, and the importance of coordinated "in situ" and remote sensing programs.

1. Introduction

While ionospheric research has been actively pursued for more than thirty years, we have yet to understand the interplay of thermospheric and magnetospheric forces in the control of ionospheric plasma distributions and electrodynamic coupling processes. The fundamental limitations in our understanding involve a grossly inadequate database to describe global distributions of electric fields, thermospheric winds, and plasma distributions. We must address these limitations and expand the database to understand ionospheric dynamics carried to the limit of unstable plasma modes and the generation of medium-to-small scale irregularities.

The ionosphere-thermosphere system responds in first order to the major driving forces of solar radiation, magnetospherically-imposed electric fields, and energetic particle precipitation. Some of these particles have direct entry from the solar wind, while others result from prompt or delayed energy transfer processes in the magnetosphere. Second and third order controls of the ionosphere and thermosphere include intricate feedback mechanisms, the streaming-, shear- and current-driven instability processes at high and equatorial latitudes, and the contributions from lower atmospheric disturbances which can propagate to altitudes above 100 km.

To fully understand the ionosphere and the solar, interplanetary, magnetospheric and thermospheric controls means that we must be able to predict the densities and heights of each ionospheric layer at any place and time, and under any condition. We must understand the processes that affect the global electrodynamic circuit through winds, electric fields and plasma layer distributions, and we must be able to predict the dynamics of the ionosphere extended to the limit of unstable geoplasma states and the specification of associated irregularity scale-size distributions.

The sections which follow will briefly review several elements in our current understanding. There will be commentary on causal relationships and ionospheric responses, with a focus on developing an understanding of "in situ" measurement requirements, parameter regimes important to ionospheric-thermospheric investigations, and the demands on spatial and temporal resolution. There will be a review of most frequently used diagnostic techniques and a discussion of future needs.

2. Perspectives on the Physical System and Measurement Requirements

2.1 The F_2 Region

The F_2 region of the ionosphere is generally thought to be laminar and quiescent except under conditions in which unstable plasma modes prevail or there are structured ionization source terms, as in the high-latitude ionosphere. A phenomenological perspective of the various domains is presented in Figure 1, with the illustration broadly intended to depict geomagnetic controls, day/night variability, and coupling to the magnetosphere. The schematic presentation is in the noon-midnight meridian, with the midnight equator at the very left of the figure, the north-polar cap in the center, and the noontime equator to the right. The figure identifies three uniquely different phenomenological domains, the equatorial, midlatitude and polar regions. We move from left-to-right in describing general characteristics of each of the domains.

The nighttime equatorial ionosphere can be made up of structures that span hundreds of kilometers to fractions of a meter [*Szuszczewicz*, 1986; *Singh and Szuszczewicz*, 1984; *Kelley et al.*, 1982]. The disturbed nighttime equatorial condition is defined as

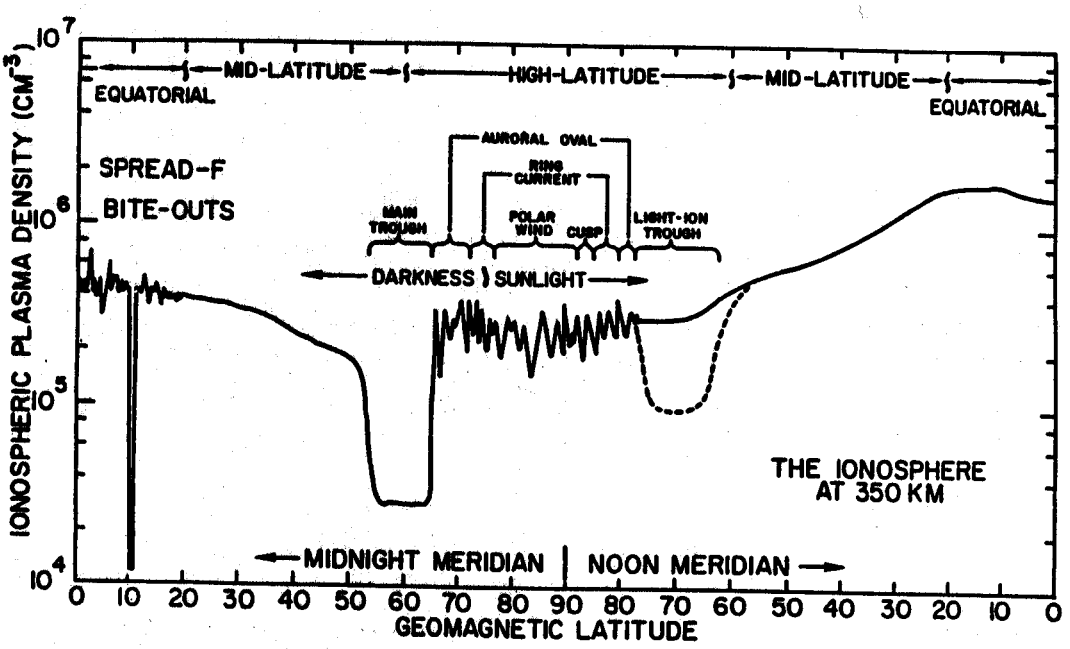

Figure 1. Phenomenological perspective of ionospheric F-region domains portrayed in a noon-midnight meridian [from *Szuszczewicz*, 1986].

equatorial spread-F (ESF) and has come to be characterized by large scale plasma "bite-outs" on the long wavelength end of the spectrum and by meter-scale radar backscatter plumes toward the shortest wavelength portion of the irregularity distribution. The bite-outs are also characterized by dramatic changes in ion composition, with O^+ the dominant ion in the high density region outside the hole, and the molecular ions NO^+ and O_2^+ dominating in lower density region within the holes. The ESF process is a nighttime phenomenon (approximately 2300 $\pm$ 300 hours local time), centered about the geomagnetic equator in a belt about $\pm 20°$ wide in latitude, with seasonal, solar-cycle, and day-to-day variations superimposed.

The generation of irregularities in ESF has been identified with a hierarchy of instability mechanisms (see *e.g.* Figures 2 and 3) generally initiated on the bottomside gradient of the F_2-layer and associated with collisional Rayleigh-Taylor and the $\vec{E} \times \vec{B}$ gradient-drift instabilities (for irregularities in the approximate range 100 m to 2 km). A full accounting of the complete irregularity distribution includes a proposed velocity-sheared Rayleigh-Taylor mechanism at longer wavelengths (1-50 km), universal drift waves at transitional dimensions (appr. 10-200 m) and an assortment of candidate processes (including the kinetic lower hybrid drift instability) in the shortest wavelength regime (< 20 m) [see, for example, *Singh and Szuszczewicz*, 1984; *Kelley et al.*, 1982; *Keskinen et al.*, 1981]. A synthesized perspective of irregularity power spectral density behavior is presented in Figure 3, showing a $k^{-1.5}$ power spectral behavior ($k = 2\pi/\lambda$) at larger wavelengths (2-60 km, the proposed velocity-sheared Rayleigh-Taylor regime), steepening to a $k^{-2.4}$ dependence at intermediate size irregularity structures (100 m to 2 km, the collisional Rayleigh-Taylor spectral region). The transitional wavelength domain (20-200 m) can steepen even further ($k^{-4.8}$ in ionospheric domains with steep density gradients), while the shortest wavelengths ($\lambda \lesssim 20$ m) manifest an almost resonant-like behavior with no systematic power law behavior. Conditions which favor the triggering of ESF include: (i) low plasma density in the field-line-coupled E and F_1 regions, (ii) high altitude for the F_2-peak, (iii) steep bottomside gradients, and (iv) an enhanced $\vec{E} \times \vec{B}$ upward drift velocity.

Irregularity distributions have also been studied in the high-latitude ionosphere where there is special focus on electrodynamics and interactive coupling with the magnetosphere and thermosphere. Unlike the equatorial region, the high-latitude ionosphere can be disturbed on a nearly 24-hour/day basis with inter-altitude coupling effects facilitated by the nearly-vertical geomagnetic fieldline structure. Plasma production at high-latitudes is the result of two sources. The first is the solar-EUV-produced component which varies smoothly across the polar cap, while the second ionization component is identified with energetic electrons which provide the zero-order source term for plasma structure. This is illustrated in the plasma density panel in Figure 4.

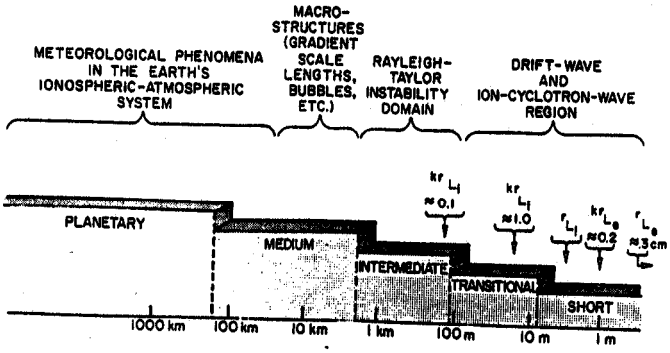

Figure 2. A simplified synoptic perspective of the full domain of equatorial F-region irregularities with potential mechanisms. Characteristic lengths are the wave number $k = 2\pi/\lambda$, and the ion and electron gyroradii r_i and r_e for $M_i = 16, T_e = 1350°K, T_i \sim 500°K$, and $B = 0.3G$ [from *Singh and Szuszczewicz*, 1984].

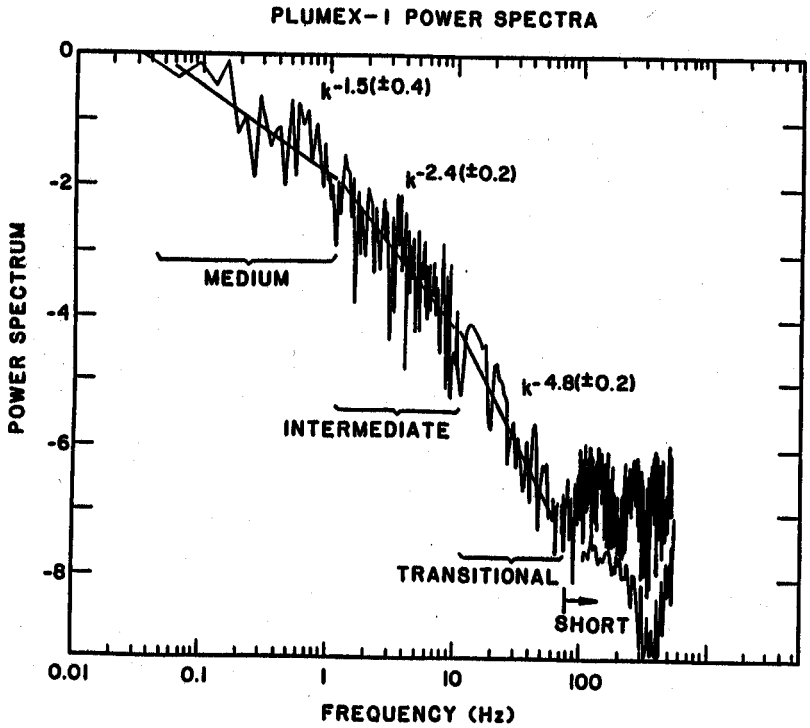

Figure 3. Power spectral distributions of equatorial spread-F irregularities from 50 km scale sizes to dimensions near 1 m. Abscissa is rocket-borne telemetry sampling rate which has a different scale-size conversion for the synthesized segments of the power spectrum. 0.1 Hz and 100 Hz correspond approximately to 20 km and 20 m, respectively [from *Singh and Szuszczewicz*, 1984].

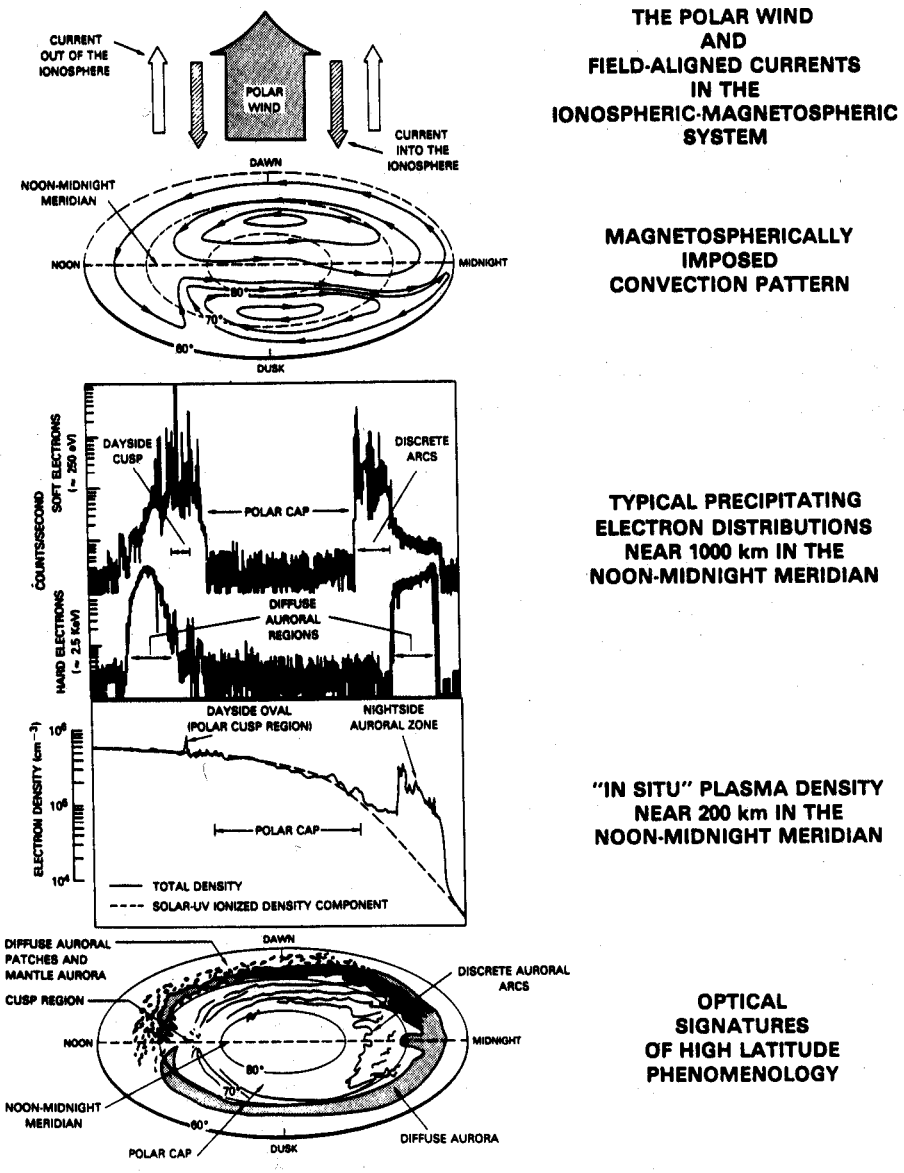

Figure 4. Composite illustration of high latitude ionospheric processes including optically-derived phenomenology, plasma density structures, precipitating particle distributions and coupling to the magnetosphere through a convective electric field, field-aligned currents and the polar wind. The format is in coordinates of magnetic local time and magnetic latitude with specific adaptations from the works of *Akasofu* [1981], *Rodriguez and Szuszczewicz* [1984], and *C. I. Meng* (private communication, 1983).

The electron precipitation at high-latitudes is variable in its energy and density distributions, horizontal extent and temporal characteristics. As a result, it creates horizontal and vertical ionospheric plasma structure by virtue of its own spatial, temporal, and energy distributions, and it provides a free energy source for a number of current-driven and two-stream ionospheric-plasma instability processes. Once created, local plasma structures are subjected to magnetic-field controls, a magnetospherically-imposed convection electric field and interactions with superimposed winds and current systems (see top panels of Figure 4).

The plasma structure produced in the high-latitude ionosphere ranges from hundreds of kilometers to meters [*Rodriguez and Szuszczewicz*, 1984; *Curtis et al., 1982*; *Huba and Ossakow,* 1980; *Keskinen and Ossakow,* 1982; *Phelps and Sagalyn*, 1976; *Rino et al.*, 1978; *Singh et al.*, 1985 and 1987; *Szuszczewicz et al.*, 1982] but unlike the situation at equatorial latitudes, concerted efforts have yet to fully characterize the spectral behavior of irregularity distributions in each of the high-latitude regions. One should expect that irregularity distributions will be different in the dawn-, dusk-, noon-, and midnight ovals, and that there will be an altitude-dependence in the spectral distributions. Some of these behaviors have been seen in S3-4 satellite "in situ" plasma density observations across the summer North Pole and winter South Pole domains (see *Szuszczewicz et al.*, 1982, for orbital details and measurement characteristics). Sample data from *Singh et al.*, 1987, are presented in Figures 5 and 6 and their review is pertinent to irregularity scale size distributions, associated global-scale transport properties, and ion-chemical controls.

North Polar ionospheric observations summarized in Figures 5 and 6 were in the molecular-ion (*i.e.*, NO^+ and O_2^+) dominated altitude region below 200 km, while the South Polar ionospheric region was sampled at somewhat higher altitudes (approximately 260 km) where O^+ tended to be the dominant constituent. These differences had a major impact on the resulting observations. Lower altitude irregularities ($\delta[NO^+]$) are shorter lived and therefore show effects of local processes; higher altitude irregularities ($\delta[O^+]$) are longer lived and can be transported large distances from their source domain. This is evident in the percent occurrence plots of Figure 5. Low altitude, $\delta[NO^+]$ irregularities are dominant in the day- and nightside oval but not in the cap, a direct result of particle precipitation morphologies. On the other hand, longer lived high altitude ($\delta[O^+]$) irregularities are transported throughout the South Polar cap and the resultant percent-occurrence plot shows no distinguishing features for any of the domains.

The differences in irregularity lifetimes are also manifested in the irregularity scale-size distributions. To demonstrate this, we focus on a synoptic perspective of the power

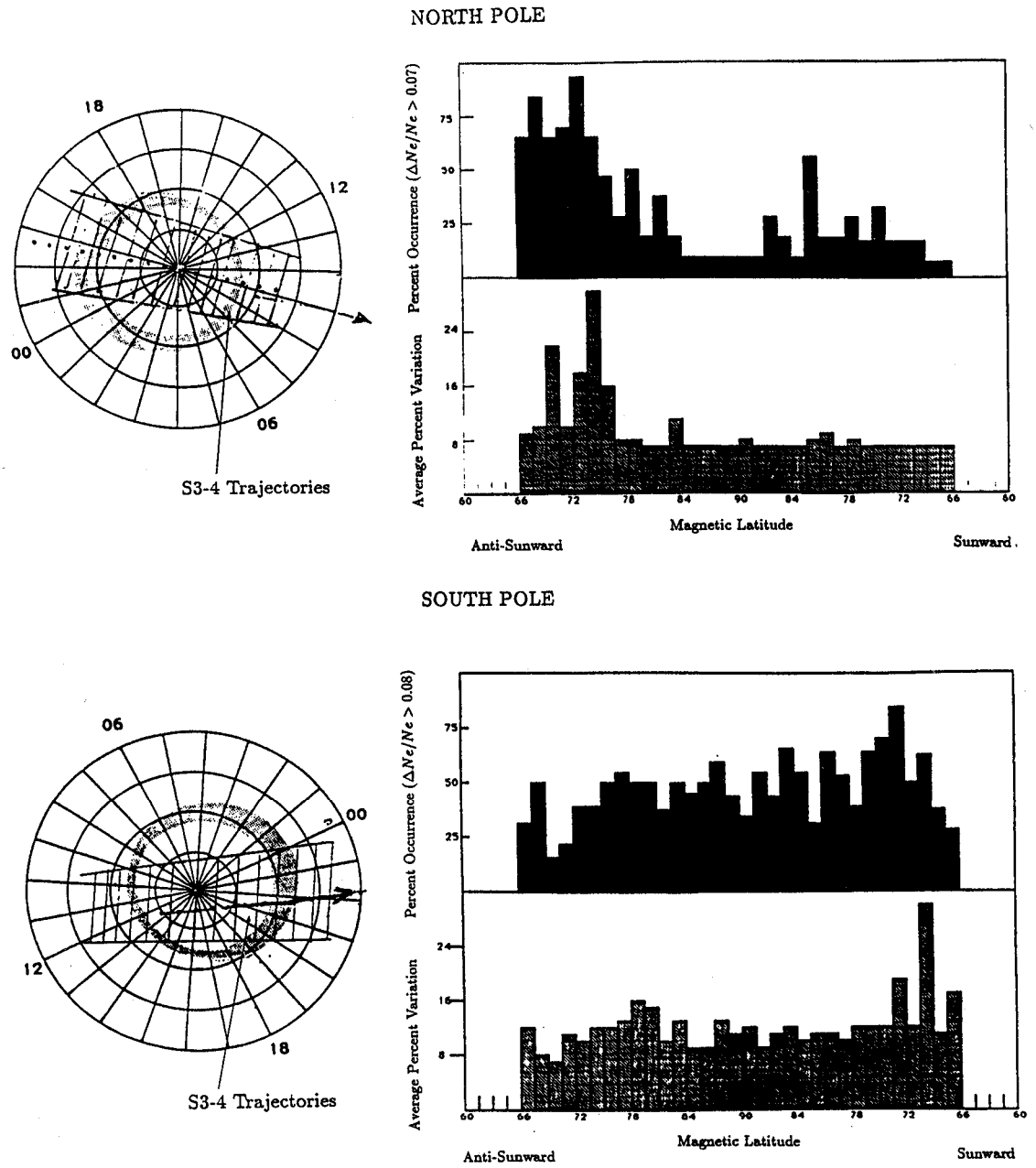

Figure 5. (Left) The S3-4 satellite trajectories used in the data analysis, with modelled oval (hatched) in MLAT-MLT coordinates. The black histogram panels show percent occurrence of density variations greater than 7%, and the gray histogram panels show averaged percent-variations of electron densities. Both histograms show the dependence on magnetic latitude [from *Singh et al.* (1987)].

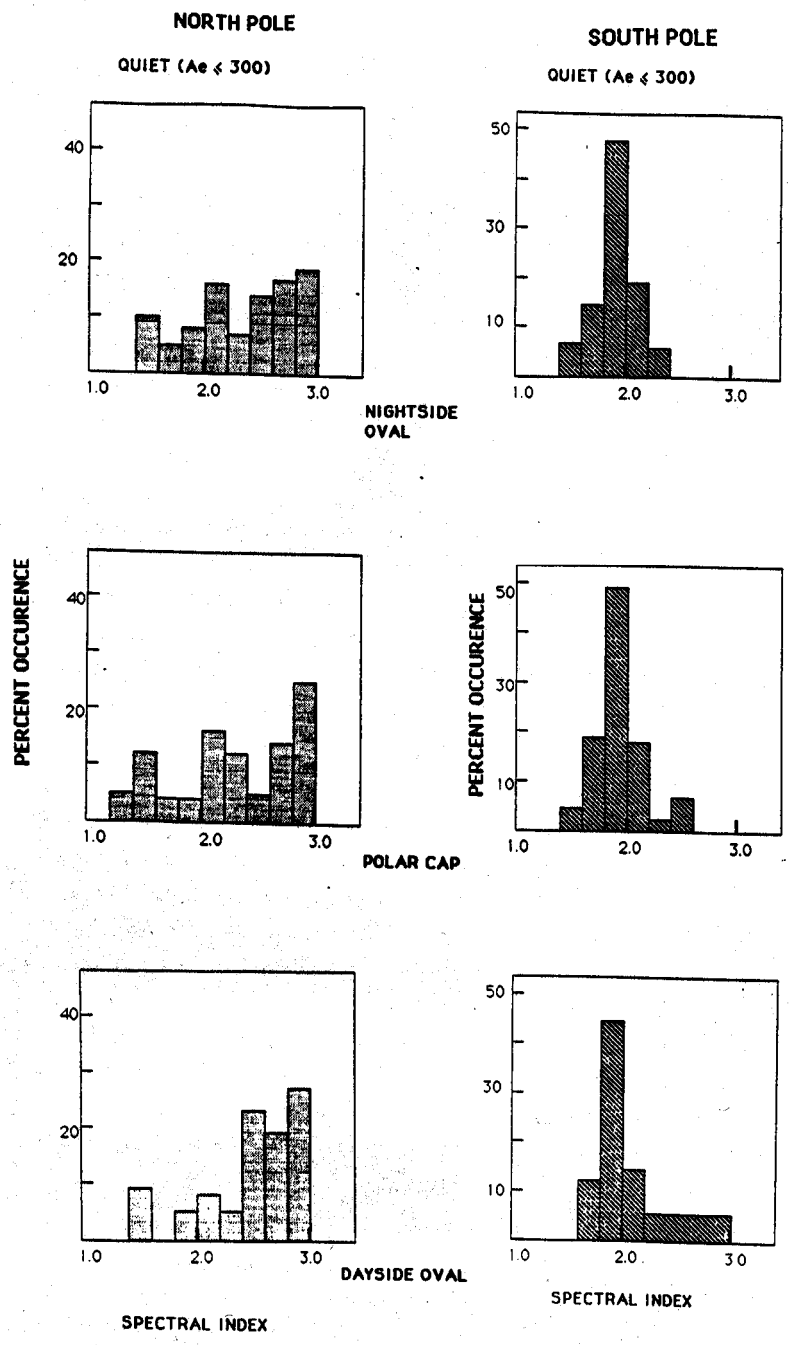

Figure 6. Percent occurrence histograms showing spectral indices for high-latitude irregularities in the nightside/dayside oval and in the polar cap under geomagnetically quiet conditions (AE<300) [adapted from *Singh et al.* (1987)].

spectral distributions of the observed irregularities ($P(k) \propto \ k^{-x} = (2\pi/\lambda)^{-x}$) in the 1-50 km wavelength regime (λ = irregularity wavelength) as published by *Singh et al.* [1987]. A typical result is presented in Figure 6, which includes histogram plots of measured spectral indices ("x" in $k^{-x} = (2\pi/\lambda)^{-x}$) in the polar cap ionosphere. The left panels of Figure 6 summarize the lower-altitude sunlit North Polar ionospheric results, while the right panel of Figure 6 summarizes the higher-altitude South Polar counterpart. The abscissa is the computer-fitted spectral index, while the ordinate is the observed frequency of occurrence. The differences across the polar regions are seen to be rather dramatic. There is a well-defined most probable spectral index at $x = 1.9$ in the higher-altitude South Polar region, while the lower-altitude North Polar data display a broad range of indices with no clearly-defined most-probable behavior. The differences can be identified with "ordered" and "unordered" plasma processes. At higher-altitudes (the data in the South Polar region), the irregularities are much longer lived and more likely to manifest susceptibility to well-defined plasma instability processes with predictable irregularity spectral distributions. On the other hand, in lower altitude regions (the data in the North Polar regions) where irregularity distributions are primarily a function of the spatial distributions of precipitating particles (largely a nondeterministic process), the spectral indices will tend to be broad ranging, without an easily-identified most-probable value. More detailed comparisons are made for each of the high-latitude domains, including the dayside and nightside ovals, in the work of *Singh et al.* [1985 and 1987].

Results like those in Figures 5 and 6 provide a database for understanding the causal mechanisms responsible for the full spectral distribution of irregularities and their global scale transport properties in the high-latitude ionosphere. But because of the near-vertical magnetic field, the complex nature of energetic-particle precipitation patterns, and the myriad of inter-altitude coupling mechanisms, substantially more work must be done, including vertical profile information from rocket-borne sensors and ground-based diagnostics. While ground-based diagnostics are site-specific, they are very useful for long-term systematic studies [*e.g.*, *Baron et al.*, 1983]. When coupled with similar diagnostic capabilities at other locations, they can also contribute to the understanding of large-scale ionospheric coupling processes and the role of longitudinal and latitudinal transport in the polar ionosphere.

2.2 The E- and F_1-Regions

The importance of winds and electric fields has long been recognized because of their roles in controlling ionospheric plasma density distributions and E- and F-region dynamics. The equatorial and low-latitude ionosphere is dominated by electric fields generated by atmospheric tidal motion in the E-region, a process referred to as the "E-

region dynamo" [see *e.g. Akasofu and Chapman,* 1982; *Hines et al.*, 1974]. While the source for these fields is in the 100-150 km region at high-middle to low-latitudes, the fields map equatorward to higher altitudes along geomagnetic fluxtubes and produce $\vec{E} \times \vec{B}$ drifts in the ionospheric plasma. These $\vec{E} \times \vec{B}$ drifts have a dominant diurnal component, reflecting a solar-diurnal tide in the E-region driven by solar heating. The dynamo system also supports horizontal currents that have latitudinal, longitudinal and seasonal variations. These current systems in first order depend on the ionospheric plasma densities and electric fields (*i.e.*, $j = \sigma E \propto neE$).

There are several serious difficulties in our understanding and modelling of the dynamo fields and current systems. First, the plasma density profiles are seldom (if ever) as clean and simple as our traditional descriptions of laminar and quiescent E and F_1 layers. This is particularly true under dynamic, unstable or otherwise irregular conditions and is most dramatically manifested at night. It can also be true under what would otherwise be considered a nominally-quiescent condition. There is also the problem involving the "anisotropic" nature of conductivities, as represented by the longitudinal σ_0, and transverse Pedersen σ_1, and Hall σ_2 contributions. Each conductivity varies differently with the altitude distributions of the ionospheric plasma, the magnetic field strength, ion composition, particle temperatures and the neutral atmospheric densities. The situation is further complicated by the fact that the electric field consists of several distinct components, such as the corotation field, the superimposed magnetospheric fields, the wind-driven dynamo fields ($\vec{E}_d = -\vec{V} \times \vec{B}$) and the polarization fields E_p. The result is a net field and a current system that depend critically on the height distributions of N_e, as reflected in the linear dependence of conductivities σ_0, σ_1 and σ_2 on the local ionospheric plasma densities [see *e.g., Akasofu and Chapman,* 1982].

Perhaps the most important conclusion to be drawn from what has been said is the globally-significant role played by winds and ionospheric plasma distributions in the 100 - 200 km altitude region. This is the source region for a dynamo-generated potential of $(10)^4$ volts with a current of $(10)^5$ amperes [*Banks et al.*, 1988]. Because the fields are carried upwards along geomagnetic fluxtubes, the winds and plasma distributions in the dynamo region can influence the dynamics at higher altitudes and at locations horizontally removed from the source region by 100's to 1000's of kilometers. The electric field coupling mechanisms operate on the remote ionospheric plasma which in turn couples to the thermosphere through ion-neutral collisions. Attempts to develop global models of these coupling processes are hampered by the fact that the 100 - 200 km regime is the least explored geoplasma domain [*Banks et al.,* 1988; *Scarf et al.*, 1988]. This region has been studied primarily by site-specific ionosonde, radar and rocket investigations, since it is generally not accessible to long-lived satellite investigations

which can provide large synoptic data profiles. The overall result is a lack of appropriate data to study this key region in the Earth's global electrodynamic circuit.

The ionospheric-thermospheric community must address the lack of data and associated lack of understanding of processes that affect the global electrodynamic circuit through winds and plasma layer distributions in the 100 - 200 km regime. There should be a focus on the development of empirical specifications of thermospheric winds and plasma layer distributions in that region, with a clear recognition that those distributions are rarely (if ever) laminar and quiescent. A simple example in support of this last statement is sporadic-E (often designated simply as Es), which has long been a recognized component of plasma distributions in the lower ionosphere. Originally thought to be a mid-latitude phenomenon driven by wind-shear convergence of long-lived metallic ions [*Whitehead*, 1970; *Matsushita and Smith*, 1972 and 1975; *Strobel*, 1974], its effect on the ionospheric height profile was considered to be largely confined to altitudes near 105 km, with Es layer-thicknesses of about 1 - 5 km and peak densities at times as great as those at the F_1 and F_2 peaks (*i.e.*, of the order of $(10)^5$ cm^{-3}). This early idea of layer height, thickness and intensity is conveniently represented in Figure 7 by the rocket data of *Szuszczewicz and Holmes* [1977] collected in the mid-latitude ionosphere above White Sands, N.M. While the rocket data presents a clear example of the Es layer parameters (providing $N_e, \delta N_e, T_e, M_i$, etc.), attempts to develop global perspectives have relied almost entirely on ionosonde measurements of critical frequencies (foEs [Hz] = $8.9(10)^3\sqrt{NmEs\ [\mathrm{cm}^{-3}]}$) and virtual heights ($h'$ Es $\approx$ hmEs near 105 km). The early studies by *E. Smith* [1957, 1961 and 1976] and *Leighton et al.* [1961] are the only efforts to date which develop such a perspective. Those studies provided maps of Es occurrence probabilities and height distributions based on monthly mean ionosonde observations. That early work and continuing rocket investigations [*Smith*, 1970; *Szuszczewicz and Takacs*, 1979] began to make it clear that the developing concept of sporadic-E was not limited to mid-latitudes but instead had a wide latitudinal extent including equatorial and high-latitude domains. Furthermore, accumulated data has made it clear that Es is not a single layer phenomena, but a process involving multiple layers of varying thicknesses, dependent upon wind-shear convergence efficiencies that extend from regions very close to the magnetic equator up to high-mid-latitudes. The data suggest that layers at or near 105 km could be part of a deterministic process involving wind shear convergence in a global system of diurnal and semi-diurnal tides. This idea is best illustrated in the work of *Shen et al.* [1976] and *Mathews and Bekeny* [1979] at the Arecibo Observatory. Figure 8 presents some of the *Shen et al.* results, where it is clear that there is a time-dependent layer-formation and transport process initiated on the bottom-side of the F_2 region. That process, believed to be driven by wind shear convergence of ambient ions, begins near 180 km with a phase

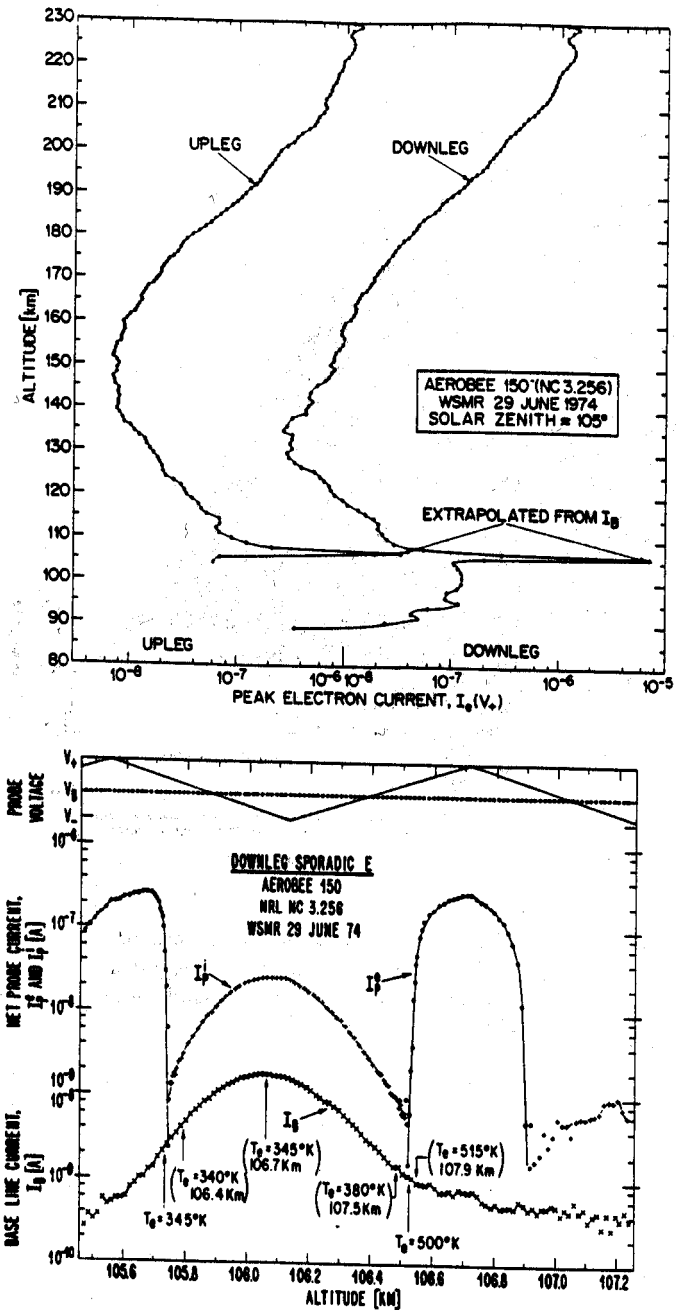

Figure 7. Electron temperature and plasma density data from a sounding rocket flight through a sporadic-E layer at WSMR, NM; top panel shows upleg and downleg total probe current ($I_e(V_+) = 10^{-5}$amp $\Rightarrow N_e \times 3(10^5)\text{cm}^{-3}$); bottom panel shows an expanded view of ion, electron and total probe current along with measured electron temperatures [from *Szuszczewicz and Holmes*, 1977].

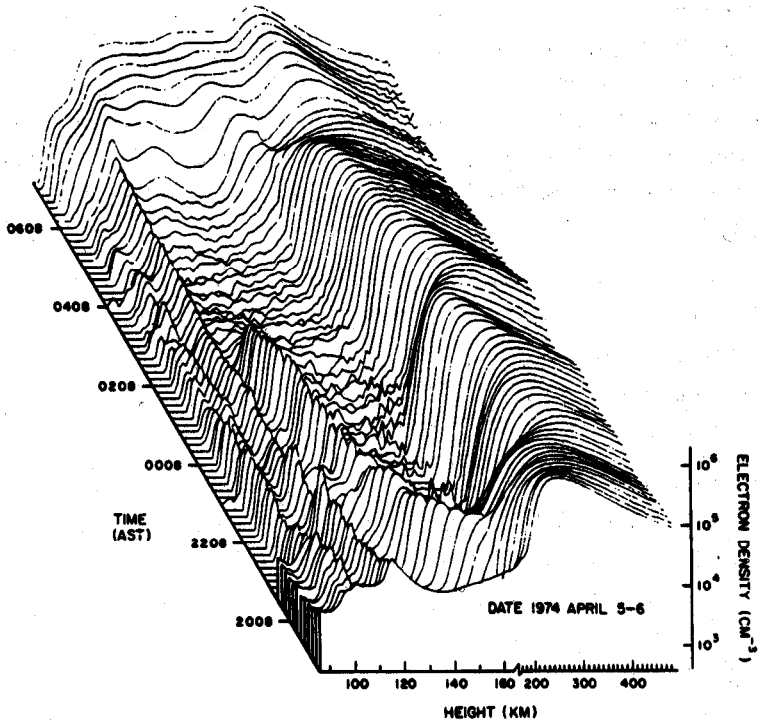

Figure 8. Arecibo incoherent scatter radar density profiles showing nighttime intermediate layer formation and descent [from *Shen et al.*, 1976].

coherent downward transport of the "collected" plasma, resulting in the formation of quasi-stationary layers in the 100 - 120 km altitude regime. The "converged" high altitude layers and their associated downward transport have given rise to the names "descending," "intermediate" and "sequential" layers; and it appears that they play an important role in the formation of "classical" low-altitude Es-layers through a process that is not "sporadic," but deterministic [*Matthews and Bekeny*, 1979]. This idea is compatable with the developing thermospheric work of R. Roble [private communication, 1989], wherein his global scale models are in concert with descending horizontal wind-shear nodes in the 100 - 200 km region. We present a selection of his results in Figure 9.

The interplay of electric and thermospheric forces in the formation and control of these ionospheric layers is both subtle and intricate. According to wind shear theory, winds alone are not the only controlling force, but instead may play an interchange role with electric fields. This is simply represented in the treatment of *Lanchester et al.* [1989] who show that the vertical ion velocity V_Z, the thermospheric wind $\vec{U}$, and local electric fields $\vec{E}$ are interrelated by the expression:

$$\left(1+\frac{\nu^2}{\omega^2}\right)V_z = \left[\frac{1}{B}\left(E_E+\frac{\nu}{\omega}E_{\perp N}\right)+\left(\frac{\nu}{\omega}U_E+U_S\sin \mathrm{I}\right)\right]\cos I+\left(\frac{\nu^2}{\omega^2}+\sin^2 I\right)U_z.$$

Accordingly, layers form at convergent nulls of the vertical ion drift V_z; *i.e.*, where $V_z = 0$ ($V_z < 0$ above and $V_z > 0$ below). Whether or not $V_z = 0$, and a convergent null is formed, depends on the horizontal neutral wind components U_E and U_S, and the electric field components E_E and $E_{\perp N}$. The subscripts E, S and $\perp N$ define directions magnetically eastward, magnetically southward, and northward and perpendicular to $\vec{B}$, respectively. Contributing terms include the ion-neutral collision frequency ν, the ion gyrofrequency ω and the dip angle I. The relative importance of the terms is readily seen to be strongly height dependent, through ν and ω. Generally speaking, $\nu < \omega$ ($\nu > \omega$) at heights above (below) 125 km.

The purpose in drawing attention to the above equation is to illustrate some of the intrinsic and subtle problems in trying to measure and model layer formation and dynamics on a global scale. We have the interplay of the wind and electric field components, complicated by a non-existent and/or impoverished database on global distributions of $\vec{E}$ and $\vec{U}$ in the altitude range in question. This problem even has serious aspects at F-region heights, where the traditional global-scale electric field model of *Richmond et al.* [1980] has been found grossly inadequate [*Szuszczewicz et al.*, 1988; *Schunk and Szuszczewicz*, 1988]. The modelling problem is further exacerbated by issues involving ion composition. Conventional wisdom has always required long-lived metallic ions to maintain the "sporadic" layers at high densities and at low altitudes.

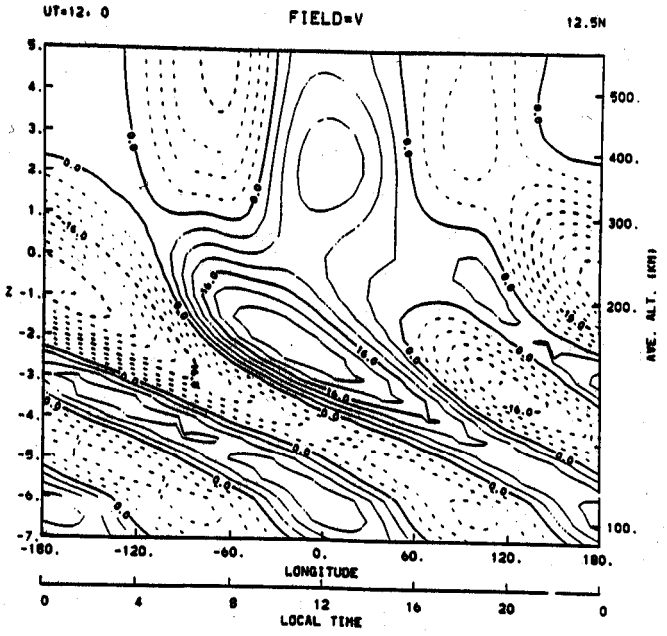

Figure 9. Meridional neutral winds from R. Roble's global thermospheric circulation model [*R. Roble*, private communication 1989]; solid contours represent northward winds, dashed contours represent southward winds at UT=12 and at 12.5° NLat.

But at F_1 and lower-F_2 heights the ion populations are dominated by O^+ and varying combinations of moleculars NO^+, O_2^+, N_2^+, NO^+, etc. Convergence and "pile-up" of moleculars would ultimately lead to their loss through increased rates of dissociative recombination; and descending layers of O^+ would see their ultimate demise through the rate-limiting reaction $O^+ + N_2 \rightarrow NO^+ + N$, and subsequent dissociative recombination of the NO^+ product. As the "intermediate" layers descend, their continued existence at high densities demands a steady accumulation of metallics while losing O^+ and the molecular ions to electron recombinations [*Mathews and Bekeny*, 1979].

The question of the overall availability of metallic ions has yet to be resolved. One might expect that semi-diurnal tidal motions might sweep the ionosphere clean of metallic ions twice a day, but *Lanchester et al.*, [1989] and *Whitehead*, [1970] suggest that meteoric input is insufficient to maintain a regular daily cycle of descending layer phenomena. There is evidence, however, that lack of phase coherence in the contributing tidal modes at altitudes near 125 km can break up the layers and redistribute the metallic ions. There is also the suggestion [*Mathews*, 1988] that the metallic ions which are swept up and deposited at altitudes below 100 km are transported equatorwards and "recycled" to the ionospheric F-region domain through the fountain effect (a well-documented and accepted process for upward transport of metallic ions at and near the equator [*Hanson et al.*, 1972; *Grebowsky and Reese*, 1989] resulting in a redistribution to higher north/south latitudes). Ultimately, however, the total metallic-ion content in the 100-200 km domain traces its origin to meteor ablations and seasonally-dependent meteor showers [*McKinley*, 1961].

These complexities make clear the current intractability of a meaningful understanding of the global distributions of the ionospheric plasma in the 100 -200 km region. There is a need for an intense measurement program to specify the forces and responses in this region of the Earth's electrodynamic circuit. Such a measurement program could provide a definitive test of the concept that "dynamic," "irregular" or otherwise "sporadic" E- and F_1 processes are part of a systematic chain of forces that involves various tidal modes of thermospheric winds (perhaps even a quarterdiurnal component [*Harper*, 1977; *Tong et al.*, 1988]), dynamo driven electric fields and ion chemistry. With this expectation, a detailed and coordinated measurement activity could hold the key to a significantly improved understanding of the ionospheric dynamo region and the ultimate treatment of the entire ionospheric domain as one dynamic and chemically-active fluid.

3. Baseline Techniques for "In Situ" Particle and Field Measurements

3.1 An Overview on Requirements

The previous sections have attempted to establish a geophysical framework for required "in situ" measurements in the ionospheric-thermospheric system. The focus was on dynamic, irregular conditions since they stress the spatial, temporal and parameter-range capabilities of any given diagnostic device. In general, if a measurement technique can meet the requirements of a dynamic environment, it can also provide the baseline data to define the zero-order, quiescent condition. This is not to underplay the importance of quiescent or moderately-dynamic states, for they define the very modes which can precipitate unstable plasma conditions and a broad range of irregularity distributions. Indeed, an accurate baseline specification of the global distribution of "quiescent" electric fields and thermospheric winds is non-existent.

The general guideline for measurement techniques therefore tends to be relatively straightforward. The parameter set must be complete (*i.e.*, we must measure all cause and effect terms, where possible); the dynamic range and accuracy must match the needs in describing the physical system; and the spatial and temporal resolution must span the range of possibilities from quiescent to fully turbulent. In general, we should measure the primary energy inputs involving solar EUV-UV radiation and the fluxes of precipitating particles at high latitudes. We must be able to measure the plasma density from 10^3 to $4(10)^6$ cm^{-3}, the electron temperature from 300-4000°K (and allow for non-Maxwellian, bi-Maxwellian or otherwise anomalous energy distributions), the electric fields from dc to approximately 50 Mhz and irregularity distributions from ten kilometer scale sizes to the meter domain. Ion composition must be resolvable from 1 - 64 amu, and ion energy determination must include the capability to detect anisotropic distributions as they can be manifested in the formation of ion conics. Ion composition measurements must also have spatial and temporal resolutions which match the prevailing conditions at high latitudes, within and across intermediate layers, and under conditions of equatorial spread-F. There are also high demands placed on the measurement of thermospheric winds. The dynamic range must run from 0 - 1000 m/sec with an accuracy approaching ± 15 m/sec and a 1 km spatial resolution over the 95-600 km altitude domain.

In what follows, we describe the "traditional" set of diagnostic techiques that have been used in accumulating the bulk of data available to date. In several circumstances we will address the issue of resolution and summarize some of the more important development requirements in the final section of this paper. Our treatment here divides the measurement techniques into three categories: (1) those which measure the state and condition of the ionosphere, (2) those which measure the state and condition of

the thermosphere, and (3) those which define energetic inputs, field controls, transport and geophysically-significant boundaries.

3.2 Measurement Techniques for the State and Condition of the Ionosphere

Langmuir-type probes. The ionospheric manifestations of ion-neutral coupling, dynamic fields, and magnetospheric inputs are embodied in the global distributions of the ion/electron densities and their associated energies. The complete specification includes not just the densities and energies, but the details of ion composition, gradient scale lengths and irregularity distributions.

In determining the state and condition of the ionosphere, the technique which appears to have received the broadest application is that of the electrostatic probe, better known as the Langmuir probe because of the pioneering work of Irving Langmuir in the first quarter of this century [*Mott-Smith and Langmuir*, 1926; *Chen*, 1965]. Langmuir probes on Explorer 22, 32 and Aloutte-II [*Brace*, 1969; *Brace et al.*, 1967;] as well as on the AE-C and DE-2 spacecraft [*Brace and Theis*, 1981; Kozura et al., 1986; *Curtis et al.*, 1985; *Fontheim et al.*, 1987] have provided much of the information available today on electron density and temperature morphologies in the global-scale ionosphere. The DE-2 Langmuir probe data also provided opportunities to study density irregularites in the wavelength interval covering 30 - 170 km in a morphological investigation that considered equatorial spread-F and high-latitude phenomenologies [*Hoegy et al.*, 1984]. A specialized Langmuir probe (referred to as a Pulsed Plasma Probe, P^3) on the S3-4 satellite complemented the DE-2 irregularity study by extending the investigation to a broader range of scale sizes, covering the full domain from 100's of km to 20 meters [*Rodriguez and Szuszczewicz*, 1984; *Singh and Szuszczewicz*, 1984; *Singh et al.*, 1987; *Szuszczewicz et al.*, 1981 and 1982].

The Langmuir probe is most simply described as a conductor (generally of planar, cylindrical, or spherical geometry) which collects current from a plasma when a voltage is applied. The current drawn from the plasma by the probe is a function of the probe size and geometry, the probe voltage, and the plasma properties of charged-particle number densities, particle distribution functions, and collision frequencies. Consequently, a current-voltage characteristic of a probe imbedded within a plasma is potentially rich with information about that plasma. If one understands the behavior of plasmas in the presence of an electrostatic probe, then in principle the plasma parameters mentioned above can be extracted from a probe characteristic.

The Langmuir probe is the smaller electrode of a two-electrode configuration (*i.e.* the probe and its reference electrode forming a closed circuit with the plasma) with the ratio of the two areas approaching a value which for all practical purposes should

be considered infinite (see insert in Figure 10). In a laboratory situation the reference electrode can, in fact, be the container of the plasma volume, while in a spaceborne application the rocket or satellite body functions as the reference electrode. A typical spaceborne cylindrical Langmuir probe is 20 cm in length and 1 mm in diameter. When the two electrodes are in contact with a plasma, a current will pass between them which is a function of an applied voltage difference and the prevailing plasma conditions. When this current is plotted as a function of the applied voltage, the resulting curve is referred to as the probe characteristic. Figure 10 shows a schematic representation of a Langmuir-probe circuit as well as a typical I-V characteristic. In conventional analysis procedures [*Chen*, 1965] N_e is determined from the electron-saturation portion of the characteristic ($V_a >$ plasma potential), T_e is determined from the transition (retarding-field) region (floating potential $\lesssim V_a <$ plasma potential), and mean-ion-mass is determined from the ion-saturation portion of the curve ($V_a <$ floating potential).

Conventional Langmuir probes (like those on the Explorer, AE and DE series of satellites) typically employ a continuous time-dependent voltage function (*e.g.* sine wave, ramp, sawtooth, etc. as in Figure 11A) to generate current-voltage (I-V) characteristics from which N_e, T_e, etc. are extracted. The time-honored conventional approach has broad applicability in fully-Maxwellian plasmas with a single characteristic electron temperature T_e and ion temperature T_i, and with temporal variability on time scales much larger than the period required to generate a single I-V characteristic. When these conditions are violated, more sophisticated approaches to Langmuir probe diagnostics are required. One such approach is that of the Pulsed Plasma Probe, P^3 [*Szuszczewicz and Holmes*, 1975; *Holmes and Szuszczewicz*, 1981]. The P^3 approach employs a series of voltage pulses ($\sim$ 100 μs wide) which follow a sawtooth envelope (see Figure 11B). During the interpulse period ($\sim$ 900 μs), the probe is held at a fixed baseline voltage level V_B which is generally positioned in the ion or electron saturation region of the probe's I-V characteristic. The long (relative to the 100 μs pulse) baseline voltage level not only stabilizes surface conditions between pulses (eliminating hysteresis effects and erroneously high measurements of electron temperature) but running measurements of baseline currents provide a measure of plasma density variations and the fundamental data for the determination of density fluctuation power spectra and associated turbulence structure [*e.g., Rodriguez and Szuszczewicz*, 1989; *Singh and Szuszczewicz*, 1984]. The continuous measurement of baseline current also allows the unfolding of a Langmuir I-V characteristic when density variations occur on a time scale short compared to the probe's sweep period [*Szuszczewicz et al.*, 1979; *Szuszczewicz and Holmes*, 1977]. Such conditions would prevail as an instrumented satellite passed through a narrow auroral arc, or a rocket trajectory carried an instru-

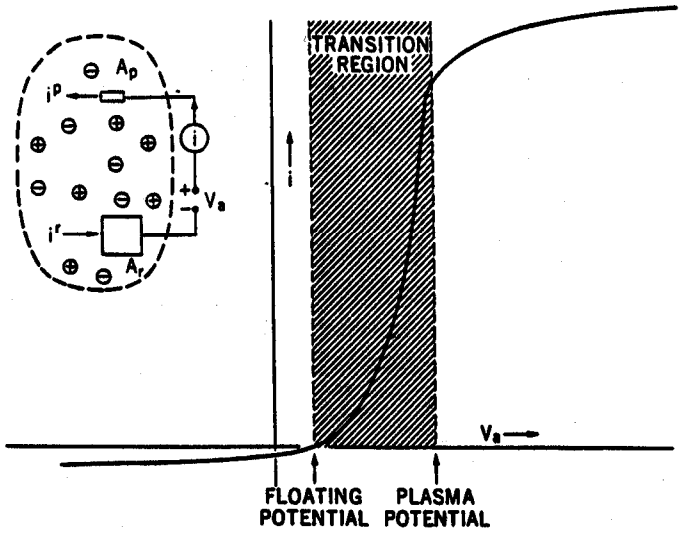

Figure 10. Schematic representation of a Langmuir probe circuit and a corresponding current-voltage characteristic [from *Szuszczewicz*, 1972].

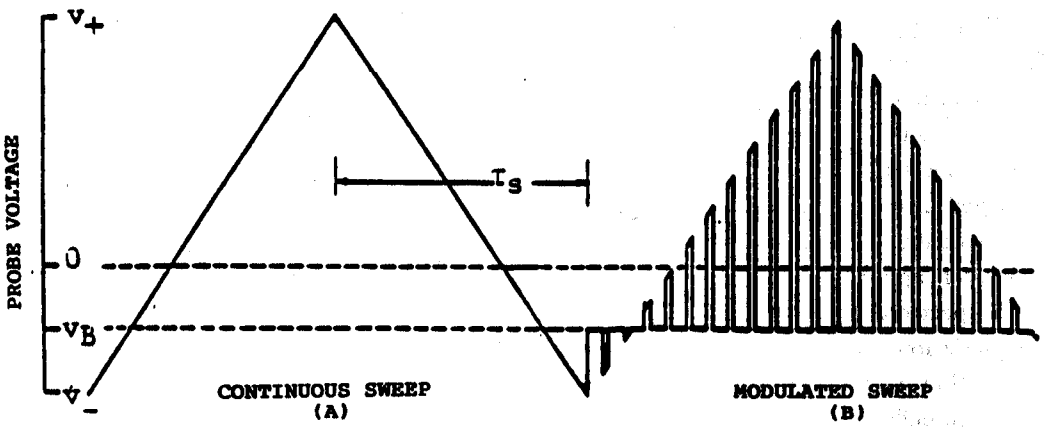

Figure 11. Continuous (panel A, the conventional Langmuir probe) and pulsed-modulated (panel B, the P^3 format) sweeps. [See *Szuszczewicz et al.*, 1982.]

mented payload through a series of narrow intermediate layers [see *e.g.* Figure 7 and *Szuszczewicz and Holmes* (1977) for P^3 measurements of T_e across narrow E_s layers].

P^3 is also unique in the measurement of multi-component electron energy distributions. This is an important issue, since it is often the experience of experimental laboratory and space plasma physics [*e.g., Szuszczewicz*, 1983] that turbulence is associated with anomalous electron energies, including bi-Maxwellian and "bump-on-tail" distributions. When irregularities exist, a conventional Langmuir I-V characteristic could not differentiate between anomalies in density variations and energy distributions. The P^3 was designed to do this. Using the baseline current levels for tracking density fluctuations in a turbulent beam-plasma interaction region, P^3 diagnosed a suprathermal electron component [*Szuszczewicz et al.*, 1983] superimposed on a cold Maxwellian in a two-stream interaction process very much like that which can occur in the high-latitude ionosphere.

If two such probes are used, their baseline voltages may be chosen to lie in the ion and electron saturation regimes, respectively. The ratio of the two baseline currents will allow rapid tracking of mean-ion-mass variations, their associated power spectral distributions and effects on instability processes [*Szuszczewicz et al.*, 1982]. This capability is expected to be of particular interest across auroral boundaries, polar cap "blobs," the mid-latitude trough, and ESF "bubbles." Useful applications also include rocket-borne diagnostics of $N_e, \delta N_e, T_e$ and δM_i in and across intermediate layers in the E and F_1-regions of the ionosphere.

Ion (and Neutral) Mass Spectrometers. While Langmuir-type probes define the state and condition of the electron component of the ionospheric plasma and its mean-ion-mass, mass spectrometers are necessary to determine the abundance of each ion species as a function of position along a satellite or rocket trajectory. Unlike the Langmuir probe sensor, which is a simple cylindrical, spherical or planar electrode suitably deployed in the plasma, the sensor for a mass spectrometer system is a complicated unit with its own technology. There are three basic types of mass spectrometers that have seen applications in spaceborne investigations. They include the Bennett Ion Mass Spectrometer (BIMS), the Quadrupole Ion Mass Spectrometer (QIMS), and the Magnetic Ion Mass Spectrometer (MIMS). The first two rely on mass filtering techniques that employ appropriate combinations of dc and rf fields, while the third uses magnetic deflection to separate and detect the individual ion constituents. Because of their greater flexibility, the treatment here will concentrate on the quadrupole and magnetic devices. In both cases the spectrometers can also measure the neutral mass constituents by employing an ionizing source in front of the filter unit. This can present some additional problems in ion optics, but with proper care it increases the versatility

of the device.

Figure 12A provides a schematic diagram of a QIMS (actually a QINMS, since an ionizer is included for neutral mass spectrometry measurements) and Figure 12B provides a block diagram of the associated electronics [see *Hunton et al.*, 1986, for instrument details]. Because of high vacuum requirements in the filtering unit, and the possibility of high-voltage arcing in the electronics unit and multiplier/sensor subassembly, the sensor package is divided into an evacuated section above the mounting flange and a sealed section below. The evacuated section of the detector is sealed (in this case) by a motor driven cover at the ion/neutral entrance-aperture end of the instrument. Other applications make use of a pyrotechnic device which expels the cover at orbital altitudes or at a proper altitude within a sub-orbital rocket trajectory.

The device shown in Figure 12A is sensitive to neutral and ionic species, though not simultaneously, and thus provides full spectrometric information on the ion and neutral constituents in the "ion mode" and "neutral mode," respectively. In addition to the heavy particle composition, the instrument provides a measurement of the total pressure of the neutral gas and the total density of the ion species in the neutral and ion modes, respectively. This information is provided by currents collected by a biased grid which is located between the ion source and the quadrupole rods. That grid collects a fraction of the total ion current leaving the ion source. Additional sensor capabilities come from a grid in the ion source that functions as a retarding potential analyzer (RPA).

In the ion mode, the ion attractor element is biased normally at -5 to -10 volts with respect to the spacecraft ground, in order to develop an attracting sheath to draw positive ions into the sensor. With the ionizer disabled, the attracted ions pass through the ion source and density analyzer sections and enter the quadrupole rod filtering element where programmed values for dc and rf fields allow either individual mass selectivity or an "integrated" ion mode (*i.e.*, all ions of mass greater than some pre-determined value can pass through the filter and be detected by the multiplier unit). The rf frequency is a constant value determined by several factors, including the desired mass range of the spectrometer. The magnitudes of the rf and dc components determine the mass of the ions that will have stable trajectories through the rods [*Paul et al.*, 1953, 1955 and 1958; *Dawson and Whetten*, 1969; *Bailey et al.*, 1982] and their amplitudes are varied in such a way that the rf/dc ratio is held constant. The device is basically a swept instrument, with either the value of the rf or dc voltages providing a monitor of the mass being sampled. A continuous sweep mode designed to cover the 1-64 amu range typically might require 0.5 seconds. Along a satellite trajectory at orbital velocities of 8 km/s, this would result in a complete spectrum having been

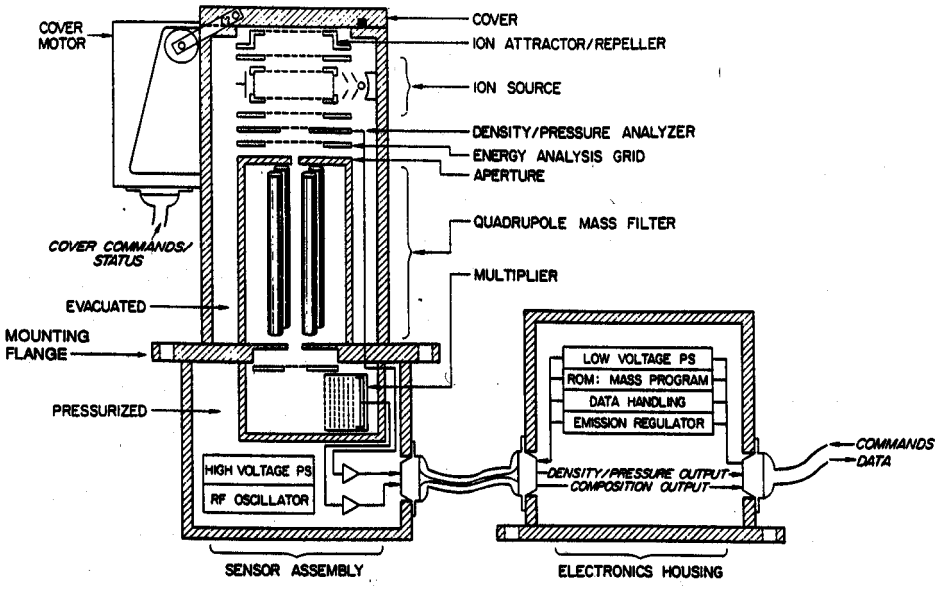

A. Schematic diagram of internal construction of QINMS

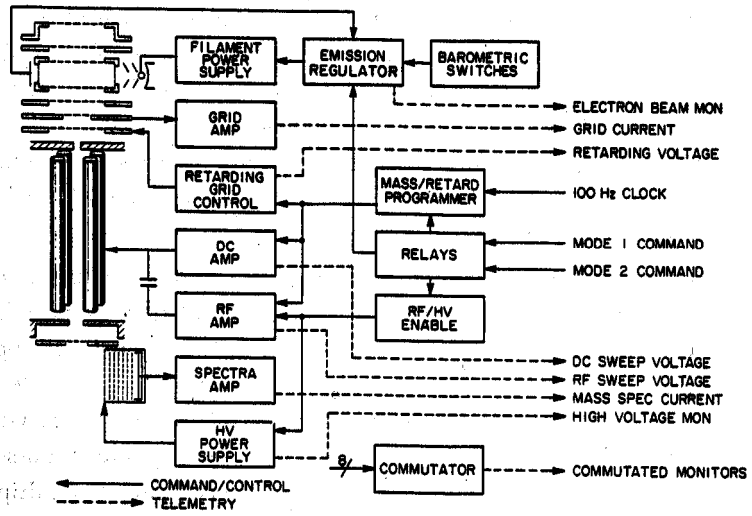

B. Block diagram of QINMS electronics

Figure 12. Schematic illustration of the Quadrupole Ion and Neutral Mass Spectrometer QINMS (Panel A) and an associated block diagram of Control Electronics (Panel B). [From *Hunton et al.*, AFGL-TR-86-0084 (7 April 1986)].

measured over a 4 km segment of the orbit. Faster sampling has been achieved by a digitally-programmed sweep which identifies pre-selected masses and samples each for a 10 ms period. In this format, for example, the device can step through O^+, N_2^+, NO^+, O_2^+ and Fe^+ in 50 ms, or an equivalent along-track distance of 400 meters. Developments in the detector system and its electronics suggest that mass dwell times could be reduced to values as low as 1 ms [*J. Ballanthin,* private conversation], providing an order of magnitude improvement in space/time resolution.

For purposes of comparison it is useful to introduce the MIMS, since it is intrinsically a faster device than the QIMS. This comparison is most easily accomplished with reference to the AE ion mass spectrometer [*Hoffmann et al.*, 1973] illustrated in Figure 13A. It is a magnetic deflection device relying on the Lorentz $\vec{V} \times \vec{B}$ force to separate the ions. It consists of an entrance aperture, an accelerator section, a magnetic analyzer, and a detector system. The electric and magnetic fields are so arranged as to produce a mass spectrum along a focal plane following the magnetic analyzer. Three slits are placed along the focal plane in appropriate places to simultaneously collect ions in the mass ratio 1:4:16. Behind each slit is an electron-multiplier log-electrometer-amplifier detector.

The diagram in Figure 13A shows the MIMS, with its entrance slit, magnet, drift tubes, exit slits, and electron multipliers. The entrance grid is a screen, which is positioned flush with the external spacecraft ground plane and electrically and thermally isolated from it. Directly behind the grid is a 2.5-cm diameter hole through a grounded plate and behind that is a small entrance slit, of approximately 0.01-cm^2 area, which forms the entrance aperture and ram inlet pumping port for the instrument package. Like the QIMS, the MIMS requires vacuum conditions in its mass analyzer.

The $\vec{V} \times \vec{B}$ mass discrimination is achieved in the analyzer magnet assembly, with a field strength of 3600 gauss in the gap, and a stray field reduced to less than 350γ at a distance 50 cm from the instrument-package center by the use of magnetic shielding materials.

Figure 13B is a block diagram showing the circuits which operate the analyzer, process the data, and interface with the spacecraft. The AE instrument operated without a conventional ion source, collecting only positive ions from the ionosphere. These were accelerated through the entrance aperture into the analyzer system by a negative sweep voltage usually with an exponential decay waveform from a programmed (resistance-capacitance decay) high-voltage power supply. As its voltage decreased, ions of progressively larger mass were successively focused on each of the three analyzer collector slits. In its fastest mode, the mass ranges 1:4, 4:16, and 16:64 amu were scanned simultaneously in the low-, mid-, and high-mass ranges, respectively, providing

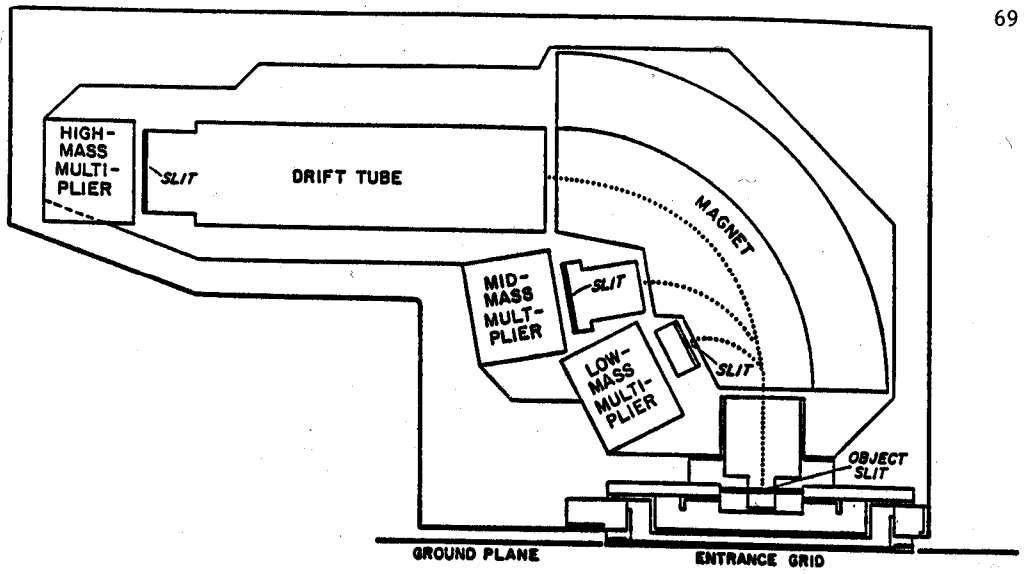

Figure 13A. Outline drawing of mass spectrometer showing entrance grid and slits. magnet with ion trajectories, collector slits, and electron multipliers. Collector slits are placed to simultaneously collect ions in the mass ratio 1:4:16. [From *Hoffman et al.*, Rad. Sci. 8, 315 (1973).]

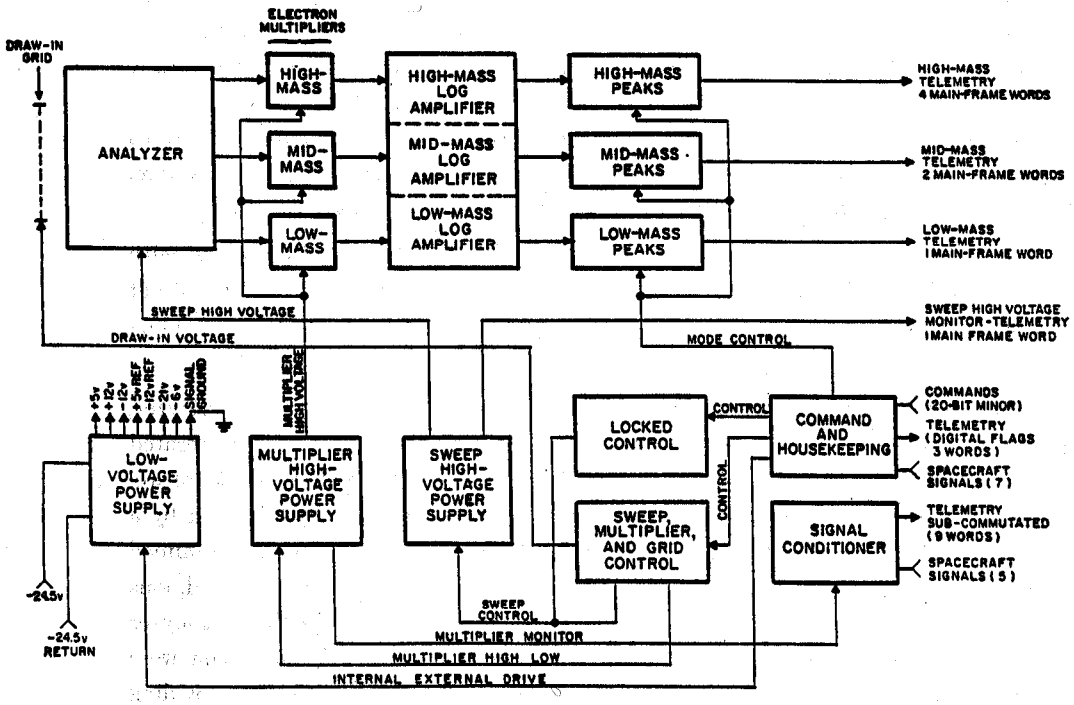

Figure 13B. Block diagram showing analyzer and electronics as well as interface with spacecraft. [From *Hoffman et al.*, Rad. Sci. 8, 315 (1973).]

the entire spectrum from 1 to 64 amu in 1 sec.

While a one sec sweep appears to be a comparatively slow rate, telemetry on the AE spacecraft was one of the major limiting factors. However, the nature of the device (not necessarily its operation on the AE spacecraft) is such that it has an intrinsically faster mass sampling capability. This faster capability is a direct consequence of the multiple-mass sensing elements arranged in a mass ratio of 1:4:16. This implies, for example, that in any 10 ms mass sampling interval, the AE-MIMS could simultaneously detect three masses. An ideal combination in the topside ionosphere would be H^+, He^+ and O^+, with the instrument providing 10 ms (80 meter) "snapshots" of the topside distribution of these light ions. This simultaneous mass sampling MIMS technique has been applied in the Giotto mass spectrometer [*Krankowsky et al.*, 1981] where five simultaneous mass ratios are sampled. The technique can be pushed even further using planar channel electron multiplier arrays for an instantaneous mass spectrum over the 1 to 64 amu range.

Retarding Potential Analyzer (RPA). The ion temperature is the remaining parameter necessary to define the complete state and condition of the ionospheric plasma. The instrument which has contributed most in specifying the thermal ion energies is the retarding potential analyzer (RPA), with a lineage going back almost 30 years [*Hanson and McKibbin*, 1961; *Hanson et al.*, 1970 and 1973]. Applications have included rockets, several Air Force satellites, and the OGO-6, Viking, Atmosphere Explorers C, D, and E, and the DE-2 spacecraft. Initially the RPA was used to measure the ion concentration (N_i) and ion temperature (T_i). In satellite applications it can also sort N_i into its constituent parts if the various ions present have widely different masses. For example, at appropriate flux levels it could identify contributions to its collected current from O^+, NO^+ and Fe^+, but it cannot separate N_2^+, NO^+ and O_2^+, nor can it identify minor constituents. Tests with the OGO-6 data also revealed the capability for measuring the bulk ion velocity component normal to the sensor face.

Illustrated in Figure 14 is the RPA on the DE-2 spacecraft [*Hanson et al.*, 1981]. It utilizes the classical planar design which requires orientation with its front face nearly normal to the vehicle velocity vector. In this configuration, ions entering the aperture in the front face pass through a region of several gridded stages with differently applied potentials. The two entrance grids (G1) are grounded to the vehicle and surrounded by a ground plane. The next grid inward is the double retarding grid (G2) to which a time-varying voltage is applied. The suppressor grid (G3) is held at a negative potential ($\approx$ -15V) to prevent low-energy ambient electrons from reaching the collector and to prevent secondary-electron escape from the collector. The shield grid is held at spacecraft ground, and is designed to protect the collector electrometer from electrical

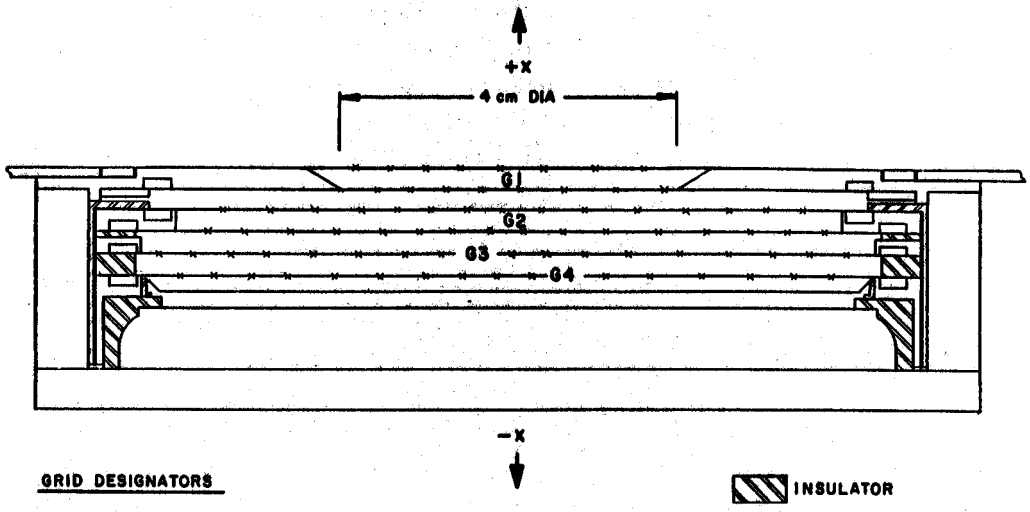

Figure 14. Schematic cross section of the DE-2 RPA sensor. The numbers in parenthesis describing the grids give the number of one mil wires per inch. The nominal grid element separation is 2.5 mm. [From *Hanson et al.*, 1981].

transients generated by changing potentials on the retarding grids.

The retarding potential (on grids G2) is variable in the range from +32 to 0 V, with sweep periods varying from 300 - 700 ms. The collected ion current corresponding to an applied retarding grid voltage is synchronously detected, amplified and filtered before being presented to the spacecraft data acquisition system. The resulting I-V characteristics represent the primary data from the RPA. Subsequently a least-squares fitting technique is used to retrieve the ion temperature, total ion concentration, information on the composition of major ions (as discussed above) and the component of the ion-drift velocity that is parallel to the sensor normal.

3.3 Techniques to Measure Thermospheric Parameters

It has been established that there is a close coupling between the neutral and ionized species in the ionosphere-thermosphere system, and accordingly measurements which define the state and condition of the charged constituents must be complemented by an equivalent set of measurements to define the thermospheric state.

The thermosphere responds dynamically to the energy and momentum sources in the solar EUV and UV wavelength regimes, to precipitating energetic particles in the auroral region, and to ion-neutral collisions. Neutrals driven by ion drag can modify the Joule heating rates which in turn can influence the neutral composition and temperature distributions and feedback into the ionosphere. Convection forces at high latitudes can drive wind systems that effect the global distribution of ionospheric electric fields. Winds in the lower ionosphere can generate dynamo fields which map equatorward along flux tubes, and these same winds can bring about complicated distributions of intermediate plasma layers at altitudes co-located with wind-shear nodes.

Prior to the AE series and DE-2 spacecraft missions, little was known about the intimate coupling between the charged and neutral species in the ionosphere-thermosphere system. In many respects the thermospheric database is still relatively primitive. We have yet to establish: (1) the seasonal, diurnal and lat/long dependencies of the thermospheric wind system, (2) the roles of the lower ionospheric dynamo under steady and dynamic conditions, (3) the roles of the diurnal and semi-diurnal tides and wind shear in controlling the plasma distributions at altitudes below 200 km, and (4) the global impact of the fossil wind system on ionospheric electric fields and associated controls of the mid- and equatorial ionosphere. ("Fossil wind" is a term coined by A. Richmond to describe thermospheric winds equatorward of a poleward retreating auroral oval.) "In situ" measurements can provide the much needed database to help resolve these issues. To understand the requirements and the complexities of the measurements, we focus here on three instruments: the Wind and Temperature Spectrometer

(WATS), the Fabry-Perot Interferometer (FPI), and the Temperature and Wind Sensor (TAWS). The FPI is an optical remote sensing technique which complements the "in situ" measurements of the WATS on the DE-2 spacecraft. The TAWS is an outgrowth of the WATS technique, designed for use on rocket and satellite investigations, and to eliminate the mass spectrometer component of the WATS configuration.

Winds and Temperature Spectrometer (WATS). The Winds and Temperature Spectrometer on the DE-2 spacecraft employs a neutral mass spectrometer as the basic diagnostic element to measure the neutral constituents and their densities relative to an upstream baffle. Currents measured in the mass spectrometer as a function of the baffle position provide information on the incident velocity vector. This adaptation of mass spectrometry to measurements of wind and temperature is a relatively recent development, first employed on the AE satellites and later in a much improved version on the DE-2 spacecraft [*Spencer et al.*, 1981 and 1982; *Wharton et al.*, 1984].

Figure 15 illustrates the basic instrument concept, showing the mass spectrometer inlet orifice and a baffle geometry. (The mass spectrometer is a quadrupole system with an antechamber to improve the accuracy of the O and O_2 density measurements. These details are not important for the description offered here, and the interested reader is referred to detailed instrument description in *Spencer et al.* [1981].) The baffle is moved across the instrument input at a distance several centimeters upstream of the input orifice. The baffle movement is done at a precisely determined speed during measurements of the abundance of the major thermospheric constituents, such as O and N_2. The exact angle at which the incoming beam of neutral particles experiences greatest reduction at the input orifice to the mass spectrometer is a function of the cross-track wind component in the plane of the baffle motion. The DE-2 WATS device employed two orthogonal baffle configurations allowing determination of the vertical and zonal (*i.e.* components horizontal and perpendicular to the orbit plane) thermospheric wind components. Shown at the right in the figure is an illustration of an observed N_2 density profile in the mass spectrometer during one pass of the baffle in front of the orifice. This instrument response comprises the basic data of the wind measurement technique. The density of only a single species is considered in the measurement procedure. That procedure focuses on the amplitude variation of density with time due to baffle modulation of the entering stream as illustrated in Figure 15. The direction of arrival of the particles, and thus the signal minimum, occurs at the point in the scan where the stream, baffle, and orifice are colinear. Taking into account the velocity and orientation of the spacecraft and the measured angle between the orifice normal and direction of the minimum, permits calculation of the wind component lying in the plane defined by satellite velocity V_{sat} and the baffle scan path. The shape of the "bite out" portion of the density curve is determined by the velocity of the spacecraft, the

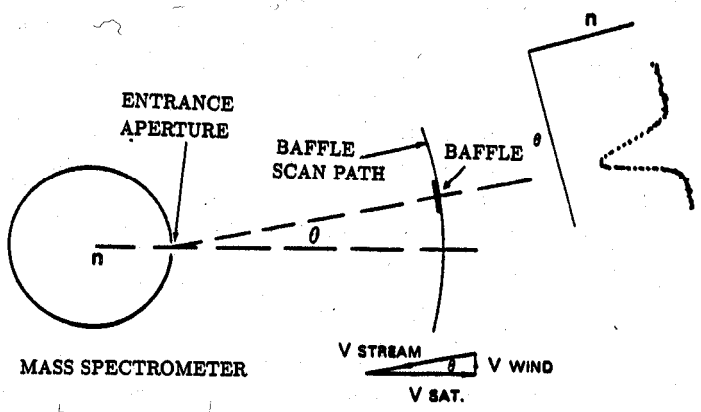

Figure 15. Schematic for the DE WATS measurement of thermospheric wind and temperature. The aperture of the closed-source mass spectrometer is scanned systematically in the vertical and horizontal planes by two baffles. (Only one baffle scan is illustrated.) As the baffle scans in front of the aperture, the measured signals drop with a characteristic signature as shown by the $n(\theta)$ plot. The baffle location at the time of maximum signal drop-off is related to the wind component in the plane of the baffle motion, and this wind can be obtained through solution of the vector triangle shown. [Adapted from *Killeen and Roble*, 1988 and *Spencer*, private communication, 1989].

scanning speed, the geometry of the baffle-orifice system, and the transverse velocity distribution (and therefore the temperature) of the N_2 particles. The gas temperature is therefore calculated from this observed density variation.

As discussed, the thermospheric wind can be obtained by solving the vector triangle shown in Figure 15. That solution requires accurate knowledge of the spacecraft velocity vector, which is obtained from a combination of horizon, Sun, and star sensor data. In the final analysis, the spacecraft velocity vector is considered to be known with sufficient precision to provide WATS wind measurements with an accuracy approaching ±15 m/s [*Killeen and Roble*, 1988].

Temperature and Wind Sensor (TAWS). While the TAWS is an outgrowth of the AE and DE-2 instruments of *Spencer et al.* [1981], it represents a completely different design which uses no moving parts, does not require a mass spectrometer, and measures the energy distribution using the established technique of electrostatic deflection [*Hanson and Heelis*, 1975; *Heelis et al.*, 1983]. The TAWS has been developed at NASA/GSFC (F. Herrero, private communication) and has had recent successes on two rocket-borne investigations. Because of its "unpublished" status, we offer a more graphic explanation of its operating principles.

Like WATS, the temperature and wind vector of the neutral atmosphere are obtained from TAWS measurements of the angle and energy distributions of the drifting Maxwellian atmospheric stream in the moving frame of the spacecraft (see Figure 16A for an overview of the measurement concept). A small aperture on the ram surface of the instrument accepts the incident stream of gas which moves supersonically with velocity $V_R = U + V_S$, V_S being the spacecraft velocity and U the wind vector. In Figure 16A ϵ defines the angle between the surface normal n and the velocity vector V_S, and θ defines the angle between V_R and V_S. Using an array of detectors which measures the angular distribution of incident particles along an arc gives $U_\perp$, the wind component perpendicular to V_R lying in the plane of the detector arc. The component $U_\parallel$ may be obtained from the energy distribution of the incident stream, in a manner similar to retarding potential analysis [*Hanson and Heelis*, 1975]. A second detector array with its arc perpendicular to the first is used to obtain the third component of the wind vector. The measured energy and angle distributions are fitted to theoretical distributions in order to obtain the wind velocity and temperature. The satellite attitude enters into the determination of $U_\perp$ through the angle ϵ in Figure 16A, with post-flight analysis of the data required to obtain an accuracy of 15-30 m/s. This represents a systematic error in $U_\perp$ only, the resolution being independent of the altitude error. $U_\parallel$, N_n and T_n are obtained directly from the distributions and are insensitive to an error in attitude as long as the instrument points within a few degrees of the ram direction (F. Herrero,

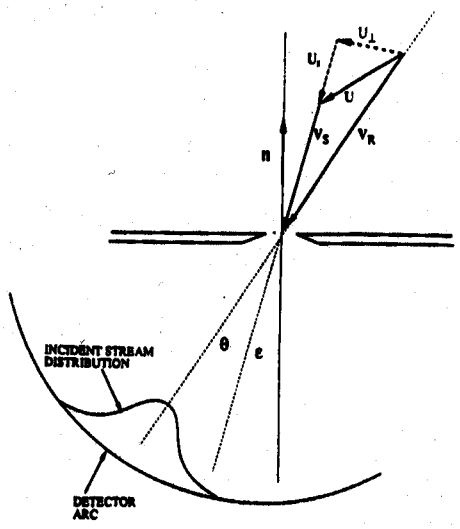

Figure 16A. Schematic description of the incident stream and the angular distribution produced in the detector arc when the satellite velocity V_S adds with the neutral wind U to give a net vector V_R at an angle θ with respect to V_S. [From *F. Herrero*, private communication.]

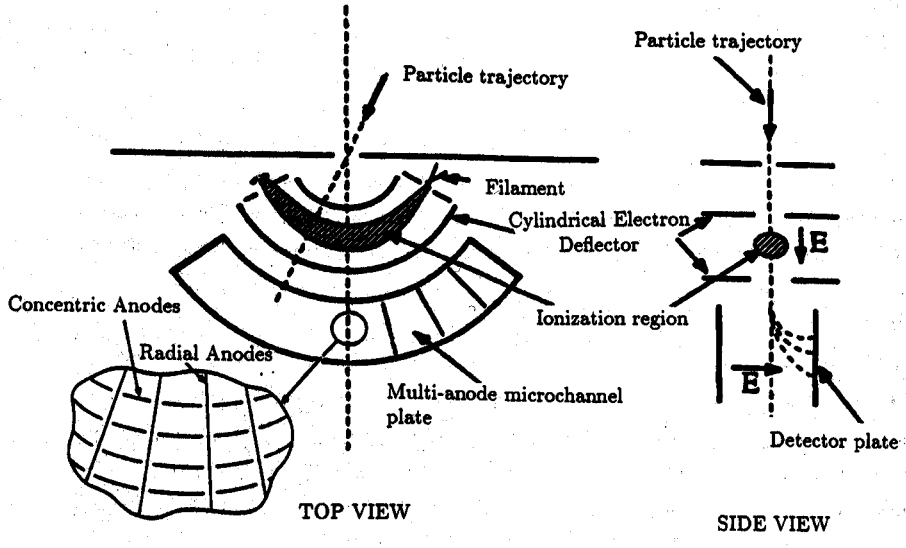

Figure 16B. Illustration of the TAWS Detector. [From *F. Herrero*, private communication.]

private communication).

Figure 16B provides a more detailed illustration of the TAWS. A 0.040 inch entrance aperture is preceded by a pair of shielded plates (not shown) which keep the ambient ions and electrons from entering the spectrometer. Once inside the detector, the neutral stream intersects an electron beam which is moving along a cylindrical electrostatic field. In that region a fraction of the neutral atoms and molecules are ionized, with some of the molecules undergoing dissociative ionization as well. In addition to maintaining the electron beam along the desired arc, the cylindrical electrostatic field withdraws the ions produced there, preserving the number density of ions at the corresponding angle of incidence. This is particularly important in contending with ions produced via dissociative ionization, which may be initially projected in a direction perpendicular to the incident molecular ray with an energy of several eV. For these ions, the radial electrostatic field rapidly deflects them in a direction closely parallel to the initial molecular ray at the corresponding angle θ. As the side view of the figure shows, the ions withdrawn from the ionization region are deflected by a constant electric field onto the detector plate. The detector is a microchannel plate with a CODACON anode structure beneath to provide the angle and energy analysis. The multiple radial anode structure shown in the inset allows 1° angular resolution over an angular range of 90° as shown. The energy analysis is achieved by the concentric arc anodes shown beneath the radial anodes in the inset. The energy resolution $\Delta E/E$ is a function of the radial position of the anode arc and is optimum for the median arc, never exceeding 0.15 based on the initial energy before acceleration out of the cylindrical field. This is sufficient in view of the natural energy spread of the incident stream. Because of the drawout field, the energy range of the analyzer extends from 0 to 20 eV. The contact potential in the analyzer may be obtained as part of least squares fit to the multiple mass peaks obtained in routine energy spectra. A TAWS flight configuration would have two mutually orthogonal sensor heads, for a full vector determination of the neutral wind velocity along the satellite track or along the trajectory of a sub-orbital rocketborne investigation.

The Fabry-Perot Interferometer (FPI). The "in situ" wind and temperature measurements of the WATS and TAWS instruments can be greatly augmented by companion remote sensing capabilities of a satellite-borne Fabry-Perot Interferometer (FPI). This was the case in DE-2 where a FPI measured altitude profiles of winds and temperatures ahead of and below the spacecraft by remotely sensing the Doppler shift and Doppler line broadening of the O(^{1}D) thermospheric emission line profile at 630 nm [*Killeen and Roble*, 1988]. The instrument field of view on DE-2 is directed along and below the spacecraft velocity vector (Figure 17), and horizon scans of the Earth's limb are performed in the orbit plane with an internal scanning mirror. The measured

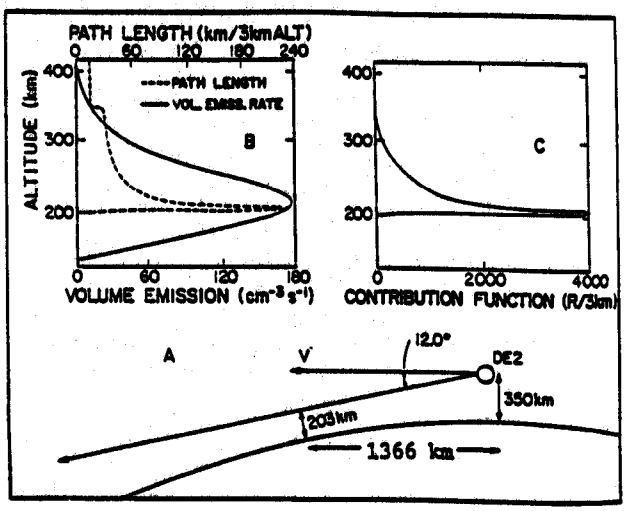

Figure 17. Typical measurement geometry for the DE/FPI (bottom schematic). The instrument performs a limb scan of the horizon, with scan angles varying between 5° and 15° from the local horizontal (shown here as 12°). A typical volume emission rate profile for the O(^{1}D) emission is shown at top left, together with a weighting function (labeled "path length") that indicates the geometrical path length through the atmosphere for the given viewing geometry shown in the figure. The contribution function (top right) is simply given by multiplying the local volume emission rate by the path length and represents the contribution to the given line-of-sight measurement from the various altitude layers. [From *Killeen and Roble*, 1988.]

Doppler shift is converted into a line-of-sight neutral wind measurement by subtracting the component of the shift due to the spacecraft velocity; and the kinetic temperature is detemined from the measured signal after subtracting the instrumental broadening function. This allows the temperature to be determined from characterization of the Gaussian half width of the emission line [*Hays et al.*, 1981; *Killeen and Hays,* 1982; *Killeen and Roble,* 1988].

The FPI measurements are spatially integrated in the (meridional) viewing direction, typically over $\sim$ 500 km or so, and the results are usually referred to the location of the tangent point along the line of sight of the instrument (see bottom panel, Figure 17) with the "contribution function" (shown in the top right panel of Figure 17 for a typical case) describing the altitudinal origin of the optical emission detected by the FPI for a given viewing geometry. For tangent point altitudes greater than the altitude of the $O(^1D)$ emission maximum, the dominant contribution to a given measurement comes from altitudes near the tangent point altitude.

While the spatial and temporal resolution of the FPI is dictated by scan time and by the integrated-field-of-view nature of the data, it represents a significant augmentation to the wind measurement of WATS. This augmentation was manifested by an analysis technique developed by *Killeen et al.* [1982] that merges the data from both instruments to provide a composite description of the horizontal neutral wind vector along the orbital track of DE-2. The technique extrapolates the remotely-sensed altitude profile of the FPI meridional wind measurements upward to the altitude of the spacecraft; and the extrapolated FPI results are merged with the "in situ" WATS zonal wind measurements to provide the summed horizontal vector wind. This superposition of data proved invaluable in mapping important phenomena in the ionosphere-thermosphere system, including geomagnetic control of winds in the polar region, characterization of the circulation patterns in the central polar cap, and ion-neutral coupling [*Killeen and Roble*, 1988; *Killeen et al.*, 1984a and b; *Killeen et al.*, 1988].

3.4 Electric and Magnetic Fields, Energetic Particles and Plasma Boundaries

In preceding sections, we have developed a baseline instrument complement capable of defining the state and condition of the ionospheric-thermospheric system. To understand those observations and fold them into the bigger picture of cause-effect relationships, we need to consider incident radiation in the UV and EUV portions of the solar spectrum, electric and magnetic fields, energetic particle inputs and plasma boundaries. We concentrate on the "in situ" measurements of energetic particles and controlling fields.

Electric Fields. Electric fields are central to the issue of "electrodynamic coupling,"

with the roles of the thermosphere and magnetosphere at the heart of the problem. A convenient (but admittedly oversimplified) view of ionospheric electric fields would identify two morphological/phenomenological domains: (1) the high-latitude domain poleward of the shielding layer (generally viewed as being near the equatorward boundary of the diffuse aurora), and (2) the remainder of the ionosphere equatorward of the auroral oval (which we refer to as the mid- and equatorial latitude region). Under quiet conditions, the magnetosphere dominates the electric field patterns at high latitudes, with ion-neutral coupling not insignificant, while the thermospheric dynamo dominates the mid- and equatorial regions, with little magnetospheric contribution. Under dynamic conditions however, the roles are intertwined at all latitudes, with no current database capable of sorting out the contributions.

The existing database on electric fields comes primarily from "in situ" differential floating potential measurements on extended booms, and from "in situ" and radar ion-drift measurements tied to $\vec{E} \times \vec{B}$ velocity effects [see *e.g. Heelis et al.,* 1981; *Heelis,* 1988]. In some regards, high-latitude electric fields have been better diagnosed and are more fully understood, but controversy still exists. Mid- and equatorial electric fields are not as well understood, with present specifications relying primarily on an empirical model developed by the incoherent radar chain in the 75° meridian [*Richmond et al.*, 1980]. Along with ground-based radars, important contributions to the current database for global electric field patterns (and the roles of the thermosphere and magnetosphere) have come from the DE investigation [see *e.g. Heelis,* 1988]. At high latitudes DE clearly showed that the time history of the field-driven convecting ions and the dynamics of the neutral gas were important to understanding the chemistry, dynamics and energy balance of the system. Unfortunately, the local time and season of the observations were locked together in a 90° inclination orbit, leaving a restricted data set and a scientific need for more comprehensive global-scale measurements.

It is clear that knowledge of the ambient electric field is vital to understanding and interpreting plasma motions, waves and turbulence at both large and small scales. DC electric field measurements are useful for studying large scale convection patterns, while wave electric fields are important in plasma instability and turbulence studies. Accordingly, electric field probes have had a long and successful flight history, beginning with simple DC instruments flown on sounding rocket and balloon payloads in the sixties [*e.g. Johnson and Kavadas,* 1963; *Mozer and Serlin,* 1969], and extending into the seventies and eighties with global-scale satellite investigations [*Maynard et al.*, 1988, *Hoffman et al.,* 1988; and *Heppner and Maynard,* 1987] and complex broadband wave analyzers in the present era of rocket-borne investigations [*e.g. Kellogg et al.*, 1986; *Kelley and Earle*, 1988].

The floating double-probe technique is by far the most common method for "in situ" electric field measurements on satellite and rocket-borne payloads, so it will be the focus of this discussion. Since only refinements in the electronics system have been made in the method since the early flight tests, much of the basic developmental work [*Fahleson,* 1967; *Mozer,* 1973] is still quite relevant today. The double-probe technique uses high-impedance difference amplifier circuits to measure the difference in the local floating potential between two small conductive probes (typically spherical in shape) that are extended on long booms from the rocket or satellite body. Since the floating potential and the local space potential in a plasma are related by a function involving the ion mass, electron temperature, and the ratio of the probe radius to the Debye length [*Szuszczewicz,* 1972] the measured floating potential difference between identical probes is proportional to the spatial electric field between them. This assumption is valid only when the ion mass, electron energy and Debye lengths are the same at each probe. These conditions are generally guaranteed to prevail in quiescent, laminar ionospheric domains, and in disturbed regions where irregularity scale sizes are much greater than the double-probe separation.

The assumption of similar plasma distributions near the two probes is implicit in the interpretation of all floating double probe measurements, and it highlights a potential limitation in dynamic, energetic and highly irregular plasma environments. Despite this necessary assumption, however, the floating double probe technique has proved extremely useful in diagnosing high- and low-latitude ionospheric electric fields [*Heppner and Maynard,* 1987; and *Maynard et al.*, 1988] and geophysical processes as diverse as two-stream and gradient-drift waves in the electrojet regions [*Pfaff et al.*, 1982; 1984], convection velocity shears [*Kelley and Carlson,* 1977; *Basu et al.*, 1988; *Earle et al.*, 1989], spread-F irregularities [*LaBelle et al.,* 1986], and lightning induced transients in the ionosphere [*Holzworth et al.,* 1985].

While measuring the potential difference between two probes is conceptually very simple, there are a variety of complications and subtleties involved in properly performing and interpreting the measurements. For example, the input impedance of the measuring circuit should be as large as possible with respect to the resistance of the plasma sheath which surrounds the probe, so that the probe electronics do not provide alternative current paths to the plasma. Input impedances of 10^{12} Ohms or more are common in modern instrumentation. It is also essential that the pair of probes used in the difference measurement be as similar as possible in size, shape, composition and distance from the spacecraft, since dissimilar sheaths, probe surface work functions, levels of surface contamination, contact potentials, wakes or current responses can introduce large errors [*Fahleson,* 1967]. In addition to using identical probes, each probe should be symmetric with respect to the boom on which it is mounted, so that

shadowing does not asymmetrically affect the photoelectron current to the probe at different portions of its spin cycle. For this reason a small tubular section of the boom is typically extended out beyond each probe, in order to cast an appropriate shadow and create symmetry with the opposing probe [*Pedersen et al.*, 1978].

By using multiple probe sets, as shown in Figure 18, the electric field in three orthogonal directions can be measured simultaneously, thereby yielding the 3-dimensional vector electric field. In practice, however, it is often difficult to measure the electric field parallel to the ambient magnetic field, since the parallel field is generally quite small in the ionosphere and the vehicle surface can interfere with the measurement when it intersects a field line which also intersects the probe [*Fahleson et al.*, 1970]. Perpendicular electric fields in the ionosphere are typically much larger, and therefore are more easily measured.

Despite these and other complexities in analysis and probe design, the floating double-probe system offers several advantages over other types of electric field instruments, such as field-mills and drift meters. One such advantage of double-probes involves the finite boom length of spinning systems which can help in determining the wavelength and propagation direction of narrowband plasma wave modes, through an interference effect known as "fingerprints" [*Temerin*, 1979; *Pfaff*, 1986]. Still another advantage exploits the Doppler shift created by the relative motion between plasma waves and the spacecraft. The Doppler shift in frequency provides phase velocity information in cases where a wave mode has a well defined fundamental frequency.

Magnetic fields. The measurement of magnetic fields is introduced into this description of "in situ" techniques not in the sense of it being a scientific objective in its own right but more in the sense of providing measurements that support other "in situ" techniques and in the sense that it aids in the overall analysis of results. Appropriate to this role is a three-axis fluxgate magnetometer with a dynamic range of $\pm$ 50,000 nT and an accuracy of 0.75 nT. At a slow sampling rate (*e.g.*, 1-5 samples/sec on each axis) the magnetometer would provide vector magnetic field measurements along the satellite track. This measurement supplies the required B-field reference for the electric field results and a corresponding baseline for $\vec{E} \times \vec{B}$ and $\vec{V} \times \vec{B}$ analysis of plasma and thermospheric wind motion and dynamo fields. At a higher sampling rate (*e.g.*, at 100 samples/sec on each axis) the instrument would provide indications of current system boundaries, a diagnostic of geomagnetic disturbances, and a monitor of Alfven and cyclotron waves (O^+ cyclotron frequency is 32 Hz in a 0.35 Gauss field). The best configuration for the magnetometer is one that allows it to be boom mounted to minimize the influence of stray fields from spacecraft systems.

Energetic particles. Next to UV and EUV portions of the solar electromagnetic

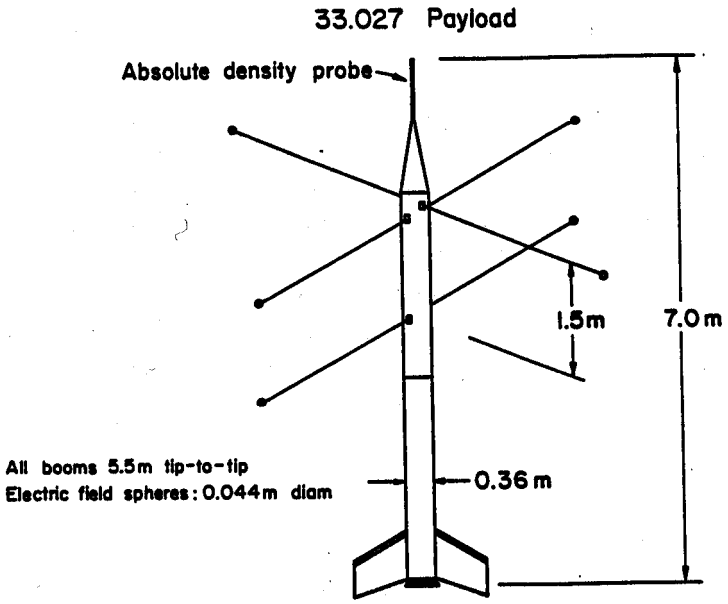

Figure 18. Sketch of payload sensor configuration drawn to scale, for including second stage motor. [Adapted from *Pfaff*, 1986.]

radiation, one of the most significant energetic inputs to the ionospheric-thermospheric system involves precipitating electrons at high latitudes. Measurement of the energy spectrum and the angular distribution of velocities with respect to the magnetic field provides the three-dimensional velocity space-distribution function for deriving the energy and momentum coupling into the ionospheric-thermospheric system.

In the past, the angular distributions of precipitating particle densities and velocities were measured by a single, narrow field-of-view analyzer on a spinning platform or by arrays of fixed, narrow field-of-view analyzers, each making a different angle with respect to the local magnetic field. Although these approaches met with reasonable success, the angular, spatial and temporal information was incomplete, and the design, packaging, and calibration of the analyzers was a difficult and costly process. For example, the plasma instrument on DE-2 required 15 collimation systems, 15 sets of deflection plates, and 15 sensors to provide the energy-angle information [*Sablik et al.*, 1988]. We describe here a "top hat"electrostatic analyzer [*Sharber et al.*, 1988], also referred to as an Angle Resolving Energy Analyzer (AREA), which alleviates this problem by using a single set of deflection plates to accept particles over a 360° field-of-view in a single plane. An early attempt at such an instrument was the quadrispheric-type analyzer, flown on the Pioneer 6 and 7 interplanetary probes [*Smith and Day*, 1971] and on the ISEE 1 and 2 satellites [*Frank et al.*, 1978]. Improvements over the quadrisphere design were achieved in the analyzers developed for applications on the AMPTE mission [*Johnstone et al.*, 1985] and on the Giotto and Suisei missions to Halley's Comet [*Johnston, et al.*, 1986; *Mukai and Miyake*, 1986].

When viewed as a symmetric quadrisphere, the top-hat instrument has its roots in a Soviet device [*Mel'nikov et al.*, 1965] flown on Cosmos 12 in 1962. Initial flight development of the 360° top-hat analyzer was accomplished by a collaborative team of investigators [*Carlson et al.*, 1983; *Paschmann et al.*, 1985] from the United States and Europe. The top-hat analyzer has now been successfully flown on the AMPTE spacecraft [*Paschmann et al.*, 1985], the Giotto mission to Halley's Comet [*Reme et al.*, 1986], and a number of sounding rockets [*e.g., Moore et al.*, 1986].

The "top-hat" electrostatic analyzer is a variation on the now commonplace spherical analyzer. The feature from which it gets its name is the small spherical section above the hemispherical deflection plates shown in the cross-sectional view of Figure 19. A charged particle entering between this top-hat and the upper hemispherical plate will be deflected into the region between the hemispherical deflection plates where (with appropriate charged-particle energies and applied fields) it will undergo "perfect" constant-radius deflection and strike the sensor (an array of eleven 16° azimuth sectors equally spaced around 360° in an equatorial acceptance plane). The device is axially

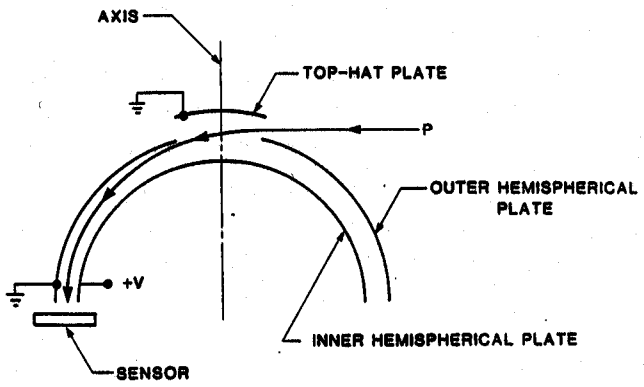

Figure 19A. Cross-sectional view of the "top-hat" electrostatic analyzer (without collimator) showing the plate arrangement and a typical particle trajectory P. For electron detection the inner hemispherical plate has deflection potential $+V$; the outer hemispherical plate and top-hat plate are grounded. [From *Sharber et al.*, 1988.]

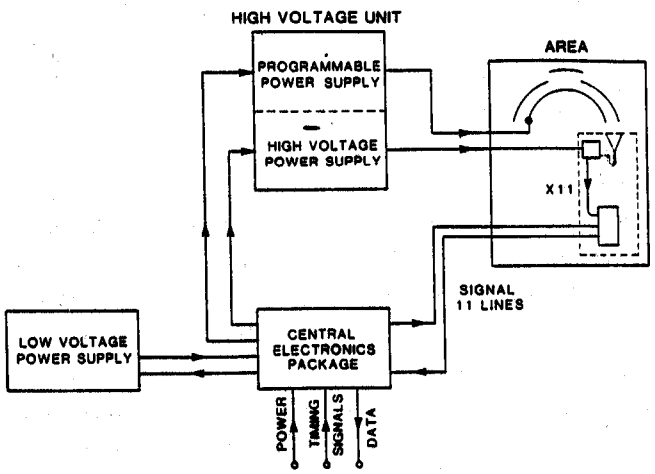

Figure 19B. Functional schematic diagram of the complete experiment showing relationships of the AREA "top-hat" deflecting and sensing unit, high-voltage unit, the low-voltage power supply, and the central electronics package. [From *Sharber et al.*, 1988.]

symmetric and therefore can provide simultaneous measurement of particles from a full 360° in the plane perpendicular to the instrument axis.

A layout of the top-hat/AREA deflection and sensor system is shown in Figure 20. The top view shows the positioning of the 11 channel electron-multiplier sensors, while the side view shows the collimator, deflection plates, and location of a channel multiplier, its amplifier, and its high-voltage biasing network. The 360° entrance aperture is defined by a series of knife-edged baffles located on the outer hemispherical plate and the top-hat plate. The baffles collimate the entrance aperture to ±7.5° with respect to the normal to the analyzer axis.

With regard to operation and control we make reference to Figure 19B. The high-voltage unit, illustrated in that figure, contains the high-voltage and programmable power supplies. The high-voltage supply provides the Channeltron bias voltage and the programmable power supply steps the voltage on the inner hemispherical plate from 2187 to 0.200 V in 59 logarithmic steps (resolving electron energies from ≈ 10 eV →≈13 keV). A time of 20 ms is required to reach and stabilize on the highest voltage and a time of 236 ms (4 ms/step) is required to cover the 59 logarithmic steps. On each step the settling time is 1.4 ms and the data accumulation time is 2.6 ms. A complete energy spectral measurement is made every 256 ms, or about every 2 km along the track of a low-Earth-orbiting satellite.

In this type of instrument, the energy and angular measurements suffer some degradation at the low energy portion of the spectrum (generally at energies < 50 eV). Several factors contribute to this, including contact potentials which introduce errors (uncertainties) in the deflection plate voltages for low particle energies, sheath effects in and around the entrance aperture which can modify the low-energy-particle orbits, and magnetic field effects which introduce Larmour orbits comparable to the radius of curvature in the deflection plate system. This latter effect has been mitigated in the top-hat AREA design by the use of mu-metal shielding [*Sharber et al.*, 1988].

If included on a polar orbiting satellite, an energetic particle detector like the "top-hat" design would provide baseline energy and momentum data for understanding high-latitude inputs to the ionosphere-thermosphere system. Covering energies from ≈ 10eV to ≈ 13 keV, it would provide full spectral information on major particle sources for energy deposition down to altitudes near 95 km, specification of the soft particle spectrum (in the polar cap), and definitive measurements of auroral oval boundaries.

4. Comments and Conclusions

While there is little doubt that an "in situ" database can provide a nearly-complete specification of cause-effect terms that define the state and condition of the ionosphere

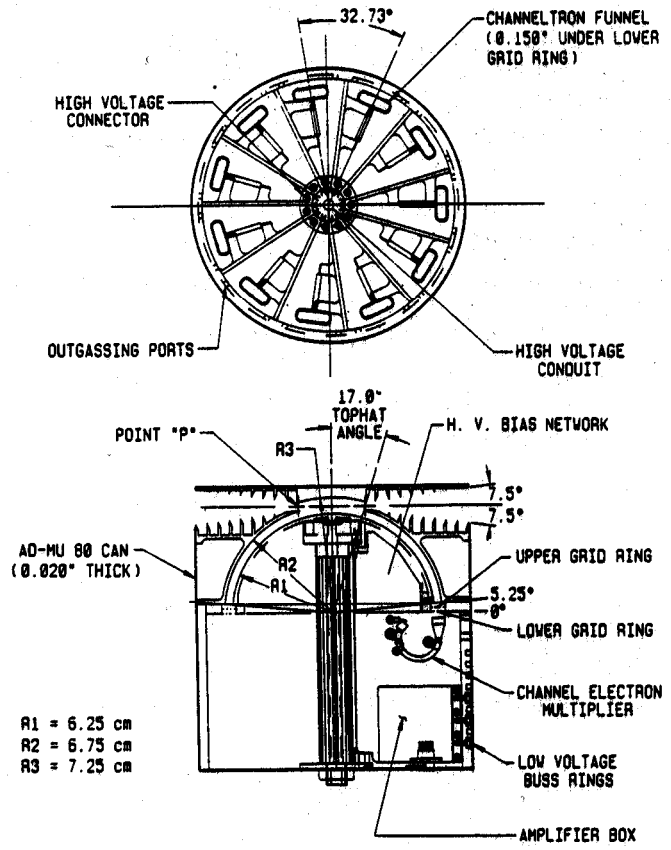

Figure 20. Layout of the "top-hat" Angle Resolving Energy Analyzer (AREA) deflection and sensing unit. [From *Sharber et al.*, 1988.]

and thermosphere, a single satellite or sub-orbital payload is limited in its ability to uniquely separate space and time variables, and develop a three-dimensional diagnosis of the interacting geospace domains. A typical approach to mitigate this problem utilizes large synoptic databases as are normally available in long-lived satellite missions. Such an approach can identify trends and ultimately specify quiescent and laminar states of global scale morphologies. More difficult, however, is the analysis of dynamic events, but there too the possibility exists for accumulating enough similar events to develop an intelligent separation of space/time controls, and integrate the results to form a three-dimensional picture. Another frequently discussed approach for future missions suggests the utilization of satellite clusters; and yet a third plan involves coordinated measurements with ground-based and "in situ" techniques. The latter possibility can be very powerful, and perhaps holds the key to solving the problem of a grossly inadequate database to define the lower ionospheric domain, its dynamo effects on the global ionosphere and its critical role in the Earth's electrodynamic circuit. The issue of intermediate layers is a case in point. Current ground-based techniques are not capable of unfolding all cause-effect terms and there are so few radar sites that a global picture cannot be developed on UT/LT, lat/long and geomagnetic controls. Satellites cannot provide a synoptic perspective in this region, and repeated multiple-site rocket launches are a financial impossibility. The solution, at least in the near term, is a coordinated ground-based and "in situ" measurement program to develop and test global-scale models that attempt to specify and predict the full system and its subsystem interactions. This is not a novel approach but one that needs to be more fully exploited to significantly advance the understanding of the ionosphere-thermosphere system and specify it as a single chemically-active and electrodynamically-responsive fluid.

Acknowledgement

I wish to extend sincere thanks to J. D. Winningham, J. Hoffman, L. Brace, W. Hanson, R. Heelis, T. Killeen, F. Herrero, J. Ballanthin and G. Earle for their inputs to the instrument descriptions. In many cases, their inputs and modified descriptions adopted from their published works were incorporated directly into the text.

References

Akasofu, S.I., Auroral arcs and auroral potential structure, in *Physics of Auroral Arc Formation,* eds. S. I. Akasofu and J.R. Kan, AGU, Washington, D.C., *Geophys. Monogr. Ser., 25*, 1, 1981.

Akasofu S.I. and S. Chapman, *Solar Terrestrial Physics*, Oxford University Press London, 1972.

Bailey, A., R. Narcisi, L. Wlodyka, G. Federico, and E. McKenna, Development of an ion mass spectrometer and sounding rocket system for D-region cluster-ion measurements, *AFGL-TR-82-0022*, AD A118752, 1982.

Banks, P., W. Roberts, and J. Kropp (eds.), Solar-Terrestrial Science Strategy Workshop, Proc. NASA/MSFC Workshop, Stanford University (September 12-16, 1988).

Baron, J.J., C.J. Heinselman and J. Petrioeks, Solar cycle and seasonal variations of the ionosphere observed with the Chatanika incoherent scatter radar, *Rad. Sci., 18*, 895, 1983.

Basu, Su., Sa. Basu, E. MacKenzie, P.F. Fougere, W.R. Coley, N.C. Maynard, J.D. Winningham, M. Sugiura, W.B. Hanson and W.R. Hoegy, Simultaneous density and electric field fluctuation spectra associated with velocity shears in the auroral oval, *J. Geophys. Res., 93*, 115, 1988.

Bering, E.A., Apparent electrostatic ion cyclotron waves in the diffuse aurora, *Geophys. Res. Lett.,* 10, 647, 1983.

Brace, L.H., B.M. Reddy and H.G. Mayr, Global behavior of the ionosphere at 1000 km altitude, *J. Geophys. Res., 72*, 265, 1967.

Brace, L.H. and R.F. Theis, Global empirical models of ionospheric electron temperature in the upper F-region and plasmasphere based on "in situ" measurements from the atmospheric Explorer-C ISIS-1 and ISIS-2 satellites, *J. Atm. Terr. Phys., 43*, 1317, 1981.

Brace, L.H., The global structure of ionospheric temperature, *12th Plenary Meeting of COSPAR (NASA X-621-69-158)*, Prague, 1969.

Carlson, C.W., D. W. Curtis, G. Paschman and W. Michael, An instrument for rapidly measuring plasma distribution functions with high resolution, *Adv. Space Res., 2*, 67, 1983.

Chen, F.F., *Plasma Diagnostic Techniques*, ed. by R.H. Huddlestone and S.L. Leonard, Academic, New York, 1965.

Curtis, S.A., W.R. Hoegy, L.H. Brace, N.C. Maynard, M. Sugiura, and J.C. Winningham, DE-2 cusp observations: role of plasma instabilities in topside ionospheric heating and density fluctuation, *Geophys. Res. Lett. 9*, 997, 1982.

Curtis, S.A., W.R. Hoegy, L.H. Brace and J.C. Winningham, Cusp altitudinal electron temperature gradient: DE-2 implications for heating mechanisms, *J. Geophys. Res., 90*, 4415, 1985.

Dawson, P.H. and N.R. Whetten, Mass spectroscopy using rf quadrupole fields, *Adv. in Electronics and Electron Phys., 27*, 59, 1969.

Earle, G.D., Electron-temperature determination in space plasmas with sounding-rocket electric field booms, *Rev. Sci. Instrum., 60*, 3076, 1989.

Earle, G.D., M.C. Kelley and G. Ganguli, Large velocity shears and associated electrostatic waves and turbulence in the auroral F-region, *J. Geophys. Res., 94*, 15321, 1989.

Fahleson, U., Theory of electric field measurements conducted in the magnetosphere with electric probes, *Space Sci. Rev., 7*, 238, 1967.

Fahleson, U.V., M.C. Kelley and F.S. Mozer, Investigation of the operation of a d.c. electric field detector, *Planet. Space Sci., 18*, 1551, 1970.

Fahleson, U.V., C.-G. Fälthammar and A. Pedersen, Ionospheric temperature and density measurements by means of spherical double probes, *Planet. Space Sci., 22*, 41, 1974.

Fontheim, E.G., L.H. Brace and J.D. Winningham, Properties of low energy electron precipitations in the cleft during periods of unusually high ambient electron temperature, *J. Geophys. Res., 92*, 267, 1987.

Frank, L.A., D.M. Yeager, H.D. Owens, K.L. Ackerson and M.R. English, *IEEE Trans. Geosci. Electron. GE-16*, 221, 1978.

Grebowsky, J.M. and N. Reese, Another look at equatorial metallic ions in the F-region, *J. Geophys. Res., 94*, 5427, 1989.

Gurnett, D.A., S.R. Mosier and R.R. Anderson, Color spectrograms of very-low-frequency Poynting flux data, *J. Geophys. Res., 76*, 3022, 1971.

Hanson, W.B. and R.A. Heelis, Techniques for measuring bulk gas-motions from satellites, *Sp. Sci. Instrum., 1*, 493, 1975.

Hanson, W.B., R.A. Heelis, R.A. Power, C.R. Lippincott, D.R. Zuccaro, B.J. Holt, L.H. Harmon and S. Sanatani, The retarding potential analyzer for dynamics Explorer B, *Sp. Sci. Instrum., 5*, 1503, 1981.

Hanson, W.B. and McKibbin, *J. Geophys. Res., 66*, 1667, 1961.

Hanson, W.B., S. Sanatani, D.R. Zuccaro and T. Flowerday, *J. Geophys. Res., 75*, 5483, 1970.

Hanson W. B., D. L. Sterling and R. F. Woodman, Source and identification of heavy ions in the equatorial F-layer, *J. Geophys. Res., 77*, 5530, 1972.

Hanson, W.B., D.R. Zuccaro, C.R. Lippincott and S. Sanatani, The retarding potential analyzer on atmospheric explorer, *Rad. Sci., 8*, 5483, 1973.

Harper, R. M., Tidal winds in the 100-200 km region at Arecibo, *J. Geophys. Res., 82*, 3243, 1977.

Hays, P.B., T.L. Killeen and B.C. Kennedy, The Fabry-Perot interferometer on dynamics explorer, *Sp. Sci. Instrum., 5*, 395, 1981.

Heelis, R.A., Studies of ionospheric plasma and electrodynamics and their application to ionosphere-magnetosphere coupling, *Rev. Geophys., 26*, 317, 1988.

Heelis, R.A., J.C. Foster, O. de la Beaujardiere and J. Holt, Multistation measurements of high-latitude ionospheric convection, *J. Geophys. Res., 88*, 121, 1983.

Heelis, R.A., W.B. Hanson, C.R. Lippincott, D.R. Zuccaro, L.H. Harmon, B.J. Holt, L.E. Doherty and R.A. Power, The ion drift meter for dynamics Explorer-B, *Sp. Sci. Instrum., 5*, 511, 1981.

Heppner, J.P. and N.C. Maynard, Empirical high-latitude electric field models, *J. Geophys. Res., 92*, 4467, 1987.

Hines, C.O. and Colleagues, The Upper Atmosphere in Motion, *Geophys. Mono., 18*, Am. Geophys. Union, Wash. D.C., 1974.

Hoegy, W.R., S.A. Curtis and L.H. Brace, Electron density irregularities observed on DE-2, in *Effects on the Ionosphere on C^3I Systems*, eds. J.M. Goodman, F.D.

Clorde, J.A. Klobuchar and H. Sorcher, Nat'l. Tech. Info. Serv., U.S. Dept. Comm., Springfield, VA 22167, 1984.

Hoegy, W.R., S.A. Curtis, L.H. Brace, N.C. Maynard and R.A. Heelis, DE observation of equatorial spread-F; evidence for drift waves, *Geophys. Res. Lett, 9*, 995, 1982.

Hoffman, J.H., W.B. Hanson, C.R. Lippincott and E.E. Ferguson, The magnetic ion-mass spectrometer on atmospheric explorer, *Rad. Sci., 8*, 315, 1973.

Hoffman, R.A., M. Sugiura, N.C. Maynard, R.M. Candy, J.D. Cravens and L.A. Frank, Electrodynamic patterns in the polar region during periods of extreme magnetic quiescence, *J. Geophys. Res., 93*, 14515, 1988.

Holmes, J.C. and E.P. Szuszczewicz, Plasma probe system with automatic sweep adjustment, *Rev. Sci. Inst., 52*, 377, 1981.

Holzworth, R.H., M.C. Kelley, C.L. Siefring, L.C. Hale and J.D. Mitchell, Electrical measurements in the atmosphere and ionosphere over an active thunderstorm: 2) Direct current electric fields and conductivity, *J. Geophys. Res., 90,* 9824, 1985.

Huba, J.D. and S.L. Ossakow, Influence of magnetic shear on the current convective instability in the diffuse aurora, *J. Geophys. Res., 85,* 6874, 1980.

Hunton, D.E., E. Trzcinski, L. Wlodyka, G. Federico and J. Dorian, Quadrupole ion/neutral mass spectrometer for space shuttle application, *AFGL-TR-86-0084*, 7 April 1986.

Johnson, D.W. and A. Kavadas, A rocket-borne electric field probe, *Can. J. Physics, 41,* 1980, 1963.

Johnstone, A., A. Coates, S. Kellock, B. Wilken, K. Jockers, W. Rosenbauer, W. Studemann, W. Weiss, V. Formisano, E. Amata, R. Cerulli-Irelli, M. Dobrowolny, R. Terenzi, A. Egidi, H. Borg, B. Hultquist, J. Winningham, C. Gurgiolo, D. Bryant, T. Edwards, W. Feldman, M. Thomsen, M.K. Wallis, L. Biermann, H. Schmidt, R. Lust, G. Haerendel and G. Paschmann, *Nature, 321*, 344, 1986.

Johnstone, A.D., S.J. Kellock, A.J. Coates, M.F. Smith, T. Booker and J.D. Winningham, *IEEE Trans. Nucl. Sci. NS-32*, 139, 1985.

Kelley, M.C. and C.W. Carlson, Observations of intense velocity shear and associated electrostatic waves and turbulence near an auroral arc, *J. Geophys. Res., 82,* 2343, 1977.

Kelley, M.C. and G.D. Earle, Upper hybrid and Langmuir turbulence in the auroral E-region, *J. Geophys. Res., 93,* 1993, 1988.

Kelley, M.C., R.C. Livingston, C.L. Rino and R.T. Tsunada, The vertical wavenumber spectrum of topside equatorial spread-F: estimates of backscatter levels and implications for a united theory, *J. Geophys. Res., 87,* 5217, 1982.

Kelley, M.C., C.E. Seyler and S. Zargham, Collisional interchange instability: 2) A comparison of the numerical simulations with the in-situ experimental data, *J. Geophys. Res., 92,* 10089, 1987.

Kellogg, P.J., S.J. Monson, W. Bernstein and B.A. Whalen, Observations of waves generated by electron beams in the ionosphere, *J. Geophys. Res., 91,* 12065, 1986.

Keskinen, M.J. and S.L. Ossakow, Nonlinear evolution of plasma enhancements in the auroral ionosphere, *J. Geophys. Res. 87,* 144, 1982.

Killeen, T.L., J.D. Craven, L.A. Frank, J.J. Ponthieu, N.W. Spencer, R.A. Heelis, L.H. Brace, R.G. Roble, P.B. Hays and G.R. Carignan, On the relationship between dynamics of the polar thermosphere and morphology of the aurora: global-scale observations from dynamics Explorers 1 and 2, *J. Geophys. Res., 93,* 2675, 1988.

Killeen, T.L., P.B. Hays, Doppler line profile analysis for a multi-channel Fabry-Perot interferometer, *Appl. Opt., 23,* 612, 1982.

Killeen, T.L., P.B. Hays, G.R. Carignan, R.A. Heelis, W.B. Hanson, N.W. Spencer and L.H. Brace, Ion-neutral coupling in the high-latitude F-region: evaluation of heating terms from dynamics Explorer 2, *J. Geophys. Res., 89,* 7495, 1984.

Kozura, J.U., L.H. Brace, T.E. Cravens and A.F. Nagy, A statistical study of the sub-auroral electron temperature enhancement using DE-2 Langmuir probe observations, *J. Geophys. Res., 91,* 270, 1986.

Krankowsky, D., P. Eberhardt, J.J. Berthelier, J.H. Hoffman, et al., The Giotto neutral mass spectrometer, *Proc. Int'l. Meeting on the Giotto Mission,* ESA SP-169, 1981.

LaBelle, J., M.C. Kelley, and C.E. Seyler, An analysis of the role of drift waves in equatorial spread-F, *J. Geophys. Res., 91,* 5513, 1986.

Lanchester, B.S., H. Rishbeth, T. Nygren, L. Jalonen and T. Turunen, Wave activity, F_1-layer disturbance and a sporadic-E layer over EISCAT, *J. Atm. and Terr. Phys., 51,* 179, 1989.

Leighton A.I., A.H. Shapley and E.K. Smith, The occurrence of sporadic-E, in *Ionospheric Sporadic-E, 2* 166, 1961.

Mathews J.D., Some aspects of metallic ion chemistry and dynamics in the mesosphere and thermosphere, in *Middle Atmosphere Programs, MAP, 25*, 228, 1988.

Mathews J.D. and F.S. Bekeny, Upper atmospheric tides and the vertical motion of ionospheric sporadic layers at Arecibo, *J. Geophys. Res., 84*, 2743, 1979.

Matsushita S. and E.K. Smith (Co-Chairmen), Third Seminar on the cause and structure of temperature latitude sporadic-E, (Logan Utah; Sept. 1971), in special issue *Radio Sci., 7*, 345, 1972.

Matsushita S. and E.K. Smith (Guest Editors), Conference on recent advances in the physics and chemistry of the E-region, (Boulder, Colorado; Aug. 1974), in special issue *Radio Sci, 10*, 229, 1975.

Maynard N.C., T.L. Aggson, F.A. Herrero and M.C. Liebrecht, Average low-latitude meridional electric fields from DE-2 during solar maximum, *J. Geophys. Res., 93*, 4021, 1988.

McKinley D.W.R., *Meteor science and engineering*, McGraw-Hill, New York, 1961.

Mel'nikov V.V., I.A. Savenko, B.I. Savin and P.I. Shavrin, *Geomag. Aeron. 5*, 107, 1965.

Moore T.E., C.J. Pollock, R.L. Arnoldy and P.M. Kintner, Preferential O+ heating in the topside ionosphere, *Geophys. Res. Lett., 13*, 901, 1986.

Mott-Smith, H. and I. Langmuir, The theory of collectors in gaseous discharges, *Phys. Rev., 28*, 727, 1926.

Mozer, F.S., Analyses of techniques for measuring DC and AC electric fields in the magnetosphere, *Space Sci. Rev., 14*, 272, 1973.

Mozer, F.S. and R. Serlin, Magnetospheric electric field measurements with balloons, *J. Geophys. Res., 74*, 4739, 1969.

Mukai T. and W. Miyake, *Rev. Sci. Instrum., 57*, 49, 1986.

Paschmann G., H. Loidl, P. Obermayer, M. Ertl, B. Laborenz, N. Sckopke, W. Baumjohann, C.W. Carlson and D.W. Curtis, The plasma instrument for AMPTE/IRM, *IEEE Trans. Geosci. Remote Sensing, GE-23*, 262, 1985.

Paul W., H.P. Rheinhard and U. von Zahn, Das elektrische massenfilter als massenpektrometer und isotopentrenner, *Z. Physik, 152*, 143-182, 1958.

Paul W. and H. Steinwedel, *Z. Naturforsch, 8a*, 448, 1953.

Paul W. and M. Raether, *Z. Physik, 140*, 262, 1955.

Pedersen, A., U. Fahleson and C.-G. Fälthammar, Determination of the ionospheric density and temperature using a double probe electric field detector, *Space Research XII,* Akademie-Verlag, Berlin, 1369, 1972.

Pedersen, A., R. Grard, K. Knott, D. Jones, A. Gonfalone and U. Fahleson, Measurements of quasi-static electric fields between 3 and 7 earth radii on GEOS-1, *Space Sci. Rev.,22,* 333, 1978.

Pfaff, R.F., Rocket studies of plasma turbulence in the equatorial and auroral electrojets, Doctoral thesis, Cornell University, Ithaca, New York, 1986.

Pfaff, R.F., M.C. Kelley, B.G. Fejer, E. Kudecki, C.W. Carlson, A. Pedersen, and B. Hausler, Electric field and plasma density measurements in the auroral electrojet, *J. Geophys. Res., 89,* 236, 1984.

Pfaff, R.F., M.C. Kelley, B.G. Fejer, N.C. Maynard, and K.D. Baker, In-situ measurements of wave electric fields in the equatorial electrojet, *Geophys. Res. Lett., 9,* 688, 1982.

Phelps A.D.R. and R.C. Sagalyn, Plasma density irregularities in the high-latitude topside ionosphere, *J. Geophys. Res., 81*, 515, 1976.

Reme H., J.A. Sauvaud, C. d'Uston, F. Coton, A. Cros, K.A. Anderson, C.W. Carlson, D.W. Curtis, R.P. Lin, D.A. Mendis, A. Korth and A.K. Richter, Comet Halley-Solar wind interaction from electron measurements aboard Giotto, *Nature, 321*, 349, 1986.

Richmond, A. D., M. Blanc, B. A. Emery, R. H. Wand, B. G. Fejer, R. F. Woodman, S. Ganguly, P. Amayenc, R. A. Behnke, C. Calderon and J. V. Evans, An empirical model of quiet-day ionosphere electric fields at middle- and low-latitudes, *J. Geophys. Res., 85*, 4658, 1980.

Rino, C.L., R.C. Livingston, and S.J. Matthews, Evidence for sheetlike auroral ionospheric irregularities, *Geophys. Res. Lett., 5*, 1039, 1978.

Rodriguez P. and E.P. Szuszczewicz, High-latitude irregularities in the lower F-region: intensity and scale-size distributions, *J. Geophys. Res., 89*, 9575, 1984.

Sablik M.J., D. Golimowski, J.R. Sharber and J.D. Winningham, Computer simulation of a 360° field-of-view "top-hat" electrostatic analyzer, *Rev. Sci. Instr., 59*, 146, 1988.

Scarf F. and Task Group on Solar Space Science (NAS/SSB), Space science in the twenty-first century: imperatives for the decades 1995 to 2015, National Academy Press, Washington, DC, 1988.

Schunk R.W. and E.P. Szuszczewicz, First-principle and empirical modeling of the global-scale ionosphere, *Ann. Geophysicae, 6*, 19, 1988.

Sharber J.R., J.D. Winningham, J.R. Scherrer, M.J. Sablik, C.A. Bargainer, P.A. Jensen, B.J. Mesh, N. Eaker and J.C. Baird, Design, construction and laterating calibration of the angle-researching energy analyzer (AREA): a "top-hat" instrument for auroral research, *IEEE Trans. on Geoscience and Rem. Sensing, 26*, 1988.

Shen J.S., W.E. Swartz and D.T. Farley, Ionization layers in the nighttime E-region valley above Arecibo, *J. Geophys. Res., 81*, 5517, 1976.

Siefring, C.L., Upward propagating electric fields from thunderstorms and VLF transmitters, Doctoral thesis, Cornell University, Ithaca, New York, 1987.

Singh, M., P. Rodriguez, and E.P. Szuszczewicz, Spectral classification of medium-scale high-latitude F-region plasma density irregularities, *J. Geophys. Res., 90*, 6525, 1985.

Singh, M., P. Rodriguez, D.N. Walker and C.S. Liu, A review of ionospheric irregularities at equatorial and high latitudes as observed by the STP/S3-4 satellite, in *The Effect of the Ionosphere on Communication, Navigation and Surveillance Systems*, J.M. Goodman, J.A. Klobuchar, R.G. Joiner, and A. Soicher, eds., U.S. Gov't. Printing Office, 539-548, 1987.

Singh, M., E.P. Szuszczewicz, Composite equatorial spread-F wavenumber spectrum from medium to short wavelength, *J. Geophys. Res., 89*, 2313, 1984.

Smith, E.K., Jr., Worldwide occurrence of sporadic-E, *National Bureau of Standards Circular, 582* U.S. Gov't Printing Office, 1957.

Smith, E.K., Jr., The occurrence of sporadic-E, in *Ionospheric Sporadic-E, 2*, 3, 1961.

Smith, E.K., Jr., World maps of Sporadic-E ($foEs > MHz$) for use in prediction of VHF oblique-incidence propagation, *OT Special Publication 76-10*, U.S. Dept. Comm/Office of Telecommunication, 1976.

Smith, L.G., A sequence of rocket observations of nighttime sporadic-E, *J. Atm. Phys., 32*, 1247, 1970.

Smith, Z.K. and J.R. Day, *Rev. Sci. Instrum., 42* 968, 1971.

Spencer, N.W., L.E. Wharton, H.B. Niemann, A.E. Hedin, G.R. Carignan and J.C. Maurer, The Dynamics Explorer wind and temperature spectrometer, *Space Sci. Instrum., 5*, 417, 1981.

Spencer, N.W., L.E. Wharton, G.R. Carignan and J.C. Maurer, Thermosphere zonal winds, vertical motions and temperature as measured from Dynamics Explorer, *Geophys. Res. Lett., 9*, 953, 1982.

Strobel, D.F., Physics and chemistry of the E-region: A review, *Radio Sci., 9,* 159, 1974.

Szuszczewicz, E.P., Area influences and floating potentials in Langmuir probe measurements, *J. Appl. Phys., 43*, 874, 1972.

Szuszczewicz, E.P., Laboratory simulations of controlled energetic electron-beam-plasma interactions in space, *AIAA Journal, 21*, 1374, 1983.

3. Szuszczewicz, E.P., Theoretical and experimental aspects of ionospheric structure: a global perspective on dynamics and irregularities, *Radio Science, 21*, 351, 1986.

Szuszczewicz, E.P., B. Fejer, E. Roelof, R. Schunk, R. Wolf, R. Leitinger, M. Abdu, B.M. Reddy, J. Joselyn, P. Wilkinson and R. Woodman, SUNDIAL: A world-wide-study of interactive ionospheric processes and their roles in the transfer of energy and mass in the Sun-Earth system, *Ann. Geophysicae, 6*, 3, 1988.

Szuszczewicz, E.P. and J.C. Holmes, Surface contamination of active electrodes in plasmas: distortions of conventional Langmuir probe measurements, *J. Appl. Phys., 46*, 5134, 1975a.

Szuszczewicz, E.P. and J.C. Holmes, A versatile plasma probe, *Rev. Sci. Instr., 46*, 592, 1975b.

18. Szuszczewicz, E. P. and J. C. Holmes, Observation of electron temperature graduate in mid-latitude Es layers, *J. Geophys. Res., 82*, 5073, 1977.

Szuszczewicz, E.P., J.C. Holmes and M. Singh, The S3-4 ionospheric satellite experiment: probe detection of multi-ion component plasmas and associated effects on instability processes, *Astrophys. Sp. Sciences, 86*, 235, 1982.

Szuszczewicz, E.P., M. Singh and J.C. Holmes, Satellite and rocket observations of equatorial spread-F irregularities; a two-dimensional model, *J. Atm. Terr. Phys., 43*, 779, 1981.

Szuszczewicz, E. P. and P. Z. Takacs, Magnetosheath effects on cylindrical Langmuir probes, *Phys. Fluid 22*, 2424, 1979.

Szuszczewicz, E.P., D.N. Walker, H.R. Anderson, and K. Papadopoulos, Suprathermal electron tail distribution in a space-simulation beam-plasma-discharge, in *Active Experiments in Space* (G. Haerendel, ed.) ESA SP-195, ESA Scientific and Technical Publications Branch, STEC, Noordwijk, Netherlands, 189, 1983.

Szuszczewicz, E.P., D.N. Walker, J.C. Holmes and H. Leinbach, Plasma diffusion in a space-simulation beam-plasma-discharge, *Geophys. Res. Lett., 6*, 201, 1979.

Temerin, M., Doppler shift effects on double-probe-measured electric field power spectra, *J. Geophys. Res., 84*, 5929, 1979.

Tong, Y., J. D., Mathews and W. P. Ying, An upper E-region quarterdiurnal tide at Arecibo?, *J. Geophys. Res., 93*, 10,047, 1988.

Wharton, L.E., N.W. Spencer and H.G. Mayr, The earth's thermospheric superrotation from Dynamics Explorer 2, *Geophys. Res. Lett., 11* 531, 1984.

Whitehead, J.D., Production and prediction of sporadic-E, *Rev. Geophys. and Space Sci., 8*, 65, 1970.